

## **Constraining the 410-km Discontinuity and Slab Structure in the Kuril Subduction Zone with TriPLICATION Waveforms**

This manuscript is a preprint and has been submitted for publication in *Geophysical Journal International* (Under Review). Please note that, despite having undergone peer-review, the manuscript has yet to be formally accepted for publication. Subsequent versions of this manuscript may have slightly different content. If accepted, the final version of this manuscript will be available via the 'Peer-reviewed Publication DOI' link on the right-hand side of this webpage. Please feel free to contact any of the authors; we welcome feedback.

1           **Constraining the 410-km Discontinuity and Slab**  
2           **Structure in the Kuril Subduction Zone with**  
3           **Triplication Waveforms**

4    Jiaqi Li <sup>1,\*</sup>, Tiezhao Bao <sup>2</sup>, Min Chen <sup>1,3,\*\*</sup>, Jieyuan Ning <sup>2</sup>, Ross Maguire <sup>1,4</sup>, Megan P.  
5    Flanagan <sup>5</sup> and Tong Zhou <sup>6</sup>

6    <sup>1</sup> Department of Computational Mathematics, Science and Engineering, Michigan State  
7    University, East Lansing, Michigan 48824, USA. E-mail: lijiaqi9@msu.edu

8    School of Earth and Space Sciences, Peking University, Beijing 100871, China.

9    <sup>3</sup> Department of Earth and Environmental Sciences, Michigan State University, East  
10   Lansing, Michigan 48824, USA. E-mail: chenmi22@msu.edu

11   <sup>4</sup> Department of Earth and Planetary Sciences, University of New Mexico, Albuquerque,  
12   NM, 87131, USA.

13   <sup>5</sup> EditSprings, Boston, MA, 02445, USA.

14   <sup>6</sup> Earth, Planetary and Space Sciences, University of California Los Angeles, CA, 90095,  
15   USA.

16

17

## 18 **SUMMARY**

19 The detailed structure near the 410-km discontinuity provides key constraints of the  
20 dynamic interactions between the upper mantle and the lower mantle through the mantle  
21 transition zone (MTZ) via mass and heat exchange. Meanwhile, the temperature of the  
22 subducting slab, which can be derived from its fast wave speed perturbation, is critical for  
23 understanding the mantle dynamics in subduction zones where the slab enters the MTZ.  
24 Multipathing, i.e., triplicated, body waves that bottom near the MTZ carry rich information  
25 of the 410-km discontinuity structure and can be used to constrain the discontinuity depth  
26 and radial variations of wave speeds across it. In this study, we systematically analyze the  
27 tradeoff between model parameters in triplication studies using synthetic examples.  
28 Specifically, we illustrate the necessity of using array normalized amplitude. Two 1-D  
29 depth profiles of the wave speed below the Tatar Strait of Russia in the Kuril subduction  
30 zone are obtained with our inversion approach applied to the dense broadband station  
31 waveforms recorded in China. We observe triplications due to both the 410-km  
32 discontinuity and the slab upper surface. Therefore, seismic structures for these two  
33 interfaces are simultaneously inverted. Our derived 410-km discontinuity depths are at  
34  $425 \pm 15$  km and  $420 \pm 15$  km, with no observable uplift. The slab upper surface is inverted  
35 to be located about 50-70 km below the 410-km discontinuity, between the depths of the  
36 1%-2% P-wave speed contours of a regional 3-D FWI model, but we find twice the wave  
37 speed perturbation amplitude. A wave speed increase of 3.9%-4.6% within the slab,  
38 compared to 2.0%-2.4% from the 3-D FWI model, is critically necessary to fit the  
39 waveforms with the shortest period of 2 seconds, indicating that high-frequency waves are  
40 required to accurately resolve the detailed structures near the MTZ.

41 Keywords: Body waves; Interface waves; Waveform inversion; Subduction zone  
42 processes

## 43 **Introduction**

44 The 410-km discontinuity defines the top of the mantle transition zone (MTZ). This  
45 interface has long been attributed to the mineralogical phase change of olivine to  
46 wadsleyite at around 410 km depth, demonstrated by laboratory experimental evidence  
47 (Ringwood 1975). The detailed structures near the 410-km discontinuity provide key  
48 constraints on the dynamic interactions between the upper and the lower mantle through  
49 the MTZ, particularly via mass and heat exchange.

50 One of the typical interactions involves cold slabs penetrating and elevating the 410-km  
51 discontinuity and carrying volatiles into the transition zone (Kawakatsu & Watada 2007).  
52 In a pure thermal environment, the topography of the discontinuity can directly reflect the  
53 temperature perturbations. That is, the topography can serve as a thermometer in the deep  
54 mantle (Vidale & Benz 1992). The 410-km discontinuity transitional thickness (i.e.,  
55 sharpness) is highly sensitive to the water content (Helffrich & Wood 1996; Van der  
56 Meijde et al. 2003), which also provides insight into the deep Earth's volatile budget  
57 (Thompson, 1992).

58 Although deep-focus earthquakes and cold temperatures in the subducting slab are  
59 associated (Isacks & Molnar 1971; Molnar et al. 1979), the mechanism for deep-focus  
60 earthquakes is still unclear. Interaction between the 410-km discontinuity and the  
61 subducting slab can help address this important question. Specifically, the 410-km

62 discontinuity topography inside the subducting slab could be used to infer the existence of  
63 a metastable olivine wedge, on the edge of which the transformational faulting from  
64 metastable olivine to wadsleyite may cause deep-focus earthquakes (Green II & Burnley  
65 1989; Kirby et al. 1991).

66 To detect and further constrain the upper mantle discontinuities, secondary seismic  
67 phases generated at the interface could be good candidates. The related methods can  
68 generally be classified into two categories: one is to use the reflected waves off the  
69 interfaces (e.g., Flanagan & Shearer 1998, 1999; Gu & Dziewonski 2002; Schmerr &  
70 Garnero 2007; Houser et al. 2008; Lawrence & Shearer 2008; Ritsema et al. 2009; Wang  
71 et al. 2017; Li et al. 2019; Tian et al. 2020; Wei et al. 2020; Guo & Zhou 2020); and the  
72 other is to use the converted wave upon transmissions at the discontinuities (e.g., Vinnik  
73 1977; Collier & Helffrich 1997; Thiriot et al. 1998; Chevrot et al. 1999; Niu et al. 2005;  
74 Ritsema et al. 2009). Although these secondary phases provide direct constraints on the  
75 discontinuities, stacking over hundreds of traces is usually necessary to enhance the  
76 visibility of these minor phases (Shearer 2000).

77 An alternative approach is to use the regional ( $10^\circ - 30^\circ$ ) multipathing seismic body  
78 waves that bottom near the interface. Unlike the phase conversions and reflections which  
79 are too weak to observe on an individual seismogram, these multipathing waves  
80 (triplications) are clearly recorded at a single station. Moreover, distinct triplication  
81 branches with different move-out slopes can be observed in record sections of dense  
82 seismic arrays.

83 Pioneering work on triplications was done by Niazi and Anderson (1965) and Johnson  
84 (1967). After that, a series of studies followed (e.g., Grand & Helmberger 1984; Tajima &  
85 Grand 1995; Brudzinski & Chen 2000; Wang et al. 2009) to derive regional 1-D upper  
86 mantle seismic structure by waveform matching between observed and synthetic  
87 seismograms. However, due to the complexity of the observed waveforms, most of these  
88 studies rely on trial-and-error approaches.

89 Some efforts towards automatic inversion have been made by employing the conjugate  
90 gradient method (Gao et al. 2006). However, for this gradient-based method, it is a  
91 challenge to find an appropriate initial model to avoid falling into local minima, especially  
92 for the complex triplication data. The exhaustive grid search has also been used, but with  
93 a reduced number of model parameters (e.g., Chu et al. 2012; Li et al. 2017).

94 With the rapid development of full-waveform inversion (FWI), triplicated waveforms  
95 have been recently incorporated into the 3-D FWI framework (Tao et al. 2018).  
96 Nevertheless, the FWI approach has only been applied to long-period data with the shortest  
97 period of  $\sim 8$ s due to the prohibitive computational cost to simulate higher frequency  
98 (shorter period) seismic waves, which consequently limits the image resolution. Also, the  
99 currently available data may still not be adequate to provide 3-D constraints of the MTZ  
100 structure. The adjoint method and its derived sensitivity kernels provide an efficient way  
101 to minimize the given misfit, especially useful in the 3-D FWI (e.g., Tromp et al. 2005;  
102 Bozdağ et al. 2016; Koroni & Trampert 2021). However, for gradient-based methods, the  
103 inverted model's quantitative uncertainty is hard to estimate, so are the potential tradeoffs  
104 between different model parameters. Therefore, 1-D simulation and inversion, with high-  
105 frequency waveform data (up to  $\sim 1$  Hz) and fewer parameters, still are complementary

106 and important in characterizing the MTZ discontinuities, especially near the turning points  
107 of seismic waves.

108 The temperature of the subducting slab is critical for understanding the mantle dynamics  
109 near the subduction zone. However, the inverted or modeled fast wave speed perturbations  
110 within the subducting slab still vary a lot amongst different studies. In the Kuril subduction  
111 zone, the global travel time tomography model (Fukao & Obayashi 2001) shows the wave  
112 speed perturbations within the slab are on the order of ~1%. Although the current regional  
113 3-D FWI model (Tao et al. 2018) shows a thinner but more strongly perturbed slab with  
114 ~2-3% wave speed increase, this value is still much smaller than ~5% wave speed increase  
115 within the slab constrained from the previous travel time (Ding & Grand 1994) or  
116 waveform modeling (Zhan et al. 2014). Whether or not and/or to what extent the  
117 perturbation of the slab is underestimated in tomographic results and deserves in-depth  
118 investigation. Wang et al. (2014) and Tao et al. (2017), through waveform modeling, have  
119 shown that the subducting slab near the turning points can influence triplicated waveforms.  
120 Therefore, with a carefully selected event and station distribution, triplication can be used  
121 to better constrain the slab structures with higher frequency waves. In this paper, we first  
122 introduce the phenomena of triplications. Then, we systematically analyze the tradeoff  
123 between model parameters, through forward modeling and waveform inversion. We also  
124 illustrate the necessity of using array normalized amplitude. Finally, we present a case  
125 study for seismic data sampling below the Tatar Strait of Russia, where triplications due to  
126 both the 410-km discontinuity and the slab upper surface are observed and incorporated in  
127 the non-gradient-based inversion. We simultaneously invert the seismic structures of these  
128 two interfaces and demonstrate that with high-frequency data (~ 2 s), full-waveform

129 inversion can accurately constrain the detailed structures of the MTZ, comparable to the  
130 findings from previous modeling studies.

### 131 **Multipathing triplicated body waves**

132 Triplications originate when seismic body waves encounter regions where wave speed  
133 increases sharply with depth (e.g., at the Moho, the 410-, or 660-km discontinuities, and  
134 the slab upper surface). Near such discontinuities or regions with steep wave speed  
135 gradients, body waves (both P and S phases) will propagate along different paths and can  
136 be observed on the regional distance seismic stations ( $10^\circ - 30^\circ$ ). An example of the ray  
137 path geometry and corresponding synthetic seismograms of P-wave triplications caused by  
138 the 410-km discontinuity is shown in Fig. 1a. To clearly present the triplicated phases, in  
139 this section we use the WKBJ code (Chapman 1978) to separately calculate each of the  
140 three branches. The synthetics are computed using the seismic reference velocity model  
141 IASP91 (Kennett & Engdahl 1991), assuming an earthquake source at 114 km depth. The  
142 three branches consist of the direct branch (AB), the reflected branch (BC), and the  
143 refracted branch (CD), which are illustrated in Fig. 1b, 1c, and 1d, respectively. We note  
144 that here we have not applied normalization to this synthetic case such that the relative  
145 amplitude variations between stations are kept. As shown in Fig. 1a, these triplicated  
146 phases provide dense samplings of the 410-km discontinuity. Since the ray paths of the  
147 different triplication branches are largely overlapping in the shallow part, the relative travel  
148 times and amplitudes of triplications can be attributed primarily to the structure near the  
149 transition zone.



## 150 **The tradeoff between model parameters**

### 151 **Discontinuity depth and wave speed above**

152 The existence of a low wave speed zone above the 410-km discontinuity, indicative of  
153 partial melting, can provide evidence for the water content in the mantle transition zone  
154 (Bercovici & Karato 2003). Some researchers using converted or transmitted phases have  
155 observed the existence of the low wave speed zone above the 410-km discontinuity in some  
156 regions (Revenaugh & Sipkin 1994; Schmandt et al. 2011; Wei & Shearer 2017). Such  
157 anomaly has also been modeled from triplication data (e.g., Song et al. 2004; Li et al. 2019;  
158 Han et al. 2021).

159 Here we perform an ideal synthetic case without noise, to test the sensitivity of  
160 triplications to the low wave speed zone above the interface. For the model setup, we keep  
161 the wave speed at 360 km, the same as the IASP91 model, and decrease the wave speed at  
162 410 km by 0.1 km/s to represent a low wave speed gradient within 50 km above the 410-  
163 km discontinuity (the red line in Fig. 2a).

164 We calculated both the travel time curves and waveforms (amplitude normalized by each  
165 trace) for this case. We note that for this modeling here and all the others in subsequent  
166 parts, we use the QSEIS program (Wang 1999) to calculate the full wavefield, instead of  
167 specified phases by the WKBJ program in Fig. 1. QSEIS uses the orthonormal propagator  
168 algorithm, a numerically more stable alternative to the reflectivity method. In addition, it  
169 can directly calculate waveforms starting from the onset time of the triplication phases  
170 instead of the origin time of the earthquake, which significantly saves computing time. As

171 shown in the travel time curves, the low wave speed zone above the discontinuity mainly  
172 affects the extension of the OB branch (the red line in Fig. 2b). Specifically, in this case,  
173 the direct waves (OB branch) terminate at a larger epicentral distance, thereby with  
174 increased OB branch's amplitude compared to the IASP91 synthetics (the shaded grey area  
175 in Fig. 2c). This phenomenon has also been observed in previous studies (e.g. Li et al. 2017;  
176 Li et al. 2019; Han et al. 2021) and has been used to detect the existence of the low wave  
177 speed zone.

178 However, other model candidates also have such equivalent behavior near cusp B. For  
179 example, we show a comparison between this model (the red line in Fig. 2a) and the other  
180 equivalent model with a depressed 410-km discontinuity but with a normal wave speed  
181 gradient as the IASP91 above the discontinuity (the blue line in Fig. 2a). The travel time  
182 curves (Fig. 2b) show that both of these two models will produce synthetics with an  
183 extended OB branch to larger epicentral distances to different extents compared to the  
184 IASP91 model. Specifically, the model with a low wave speed layer above the interface  
185 extends the OB branch to a relatively larger epicentral distance.

186 The waveforms of the OB branch from the two models, are quite similar at certain  
187 epicentral distances (the shaded gray area in Fig. 2c and Fig. 2d), indicating that the  
188 tradeoff does exist between the discontinuity depth and the wave speeds above the  
189 discontinuity. We note that the amplitude of the waveforms shows some discrepancies with  
190 the travel time curves (e.g., Fig. 2b shows that the OB branch terminates at  $21^\circ$  for the  
191 model with 15 km depression of the discontinuity, while the OB branch for the same model  
192 seems to be extending beyond  $21^\circ$ , in Fig. 2d). This inconsistency is due to two reasons.

193 The first is the difference between the ray theory and the finite frequency effect; the  
194 waveform calculated numerically, which takes the finite frequency effect into account, is  
195 more reliable and closer to the real physical situation. The second reason is from the  
196 normalization by each trace which we discuss in the next subsection.

197 This tradeoff has also been noticed and investigated in previous studies (e.g., Wang &  
198 Chen 2009; Song et al. 2004). For example, Wang and Chen (2009) analyze similar model  
199 pairs for the 660-km discontinuity and reject the model with a depressed interface based  
200 on its different slope for the OC branch in the travel time curves. According to our test,  
201 even if there are some differences for the slope of the OC branch in the travel time curves  
202 (Fig. 2b), the differences in the corresponding waveforms for the OC branch are more  
203 subtle (e.g., less than a quarter of the wavelength). The other reason why the waveforms  
204 from our two tested models look more identical is that we applied our waveform inversion  
205 code to search for the equivalent model of the one with low wave speed above the  
206 discontinuity (out of 15,000 models). Song et al. (2004) also discuss these two endmember  
207 models for the 410-km discontinuity by comparing the waveforms. The model with a  
208 depressed interface is ruled out due to its failure to generate the visible waveforms of the  
209 OB branch (Song et al. 2004). However, the proposed model in our case can generate a  
210 clear OB branch whose amplitude is equivalent to the model with a low wave speed zone  
211 above the interface. This discrepancy could partly come from the different earthquake  
212 sources we choose (different depths and focal mechanisms). The other possibility is that  
213 our synthetic model has an extra localized high wave speed anomaly below the interface.  
214 Assuming that this anomaly doesn't exist in the MTZ, the CD branch will be delayed. Thus,

215 if viewed in the velocity seismograph (e.g., Song et al. 2004), the negative pulses of the  
216 delayed CD branch will partly overlap with the OB branch and lower its amplitude.

217 We also note that this equivalent model we propose might not be consistent with other  
218 constraints in certain regions (e.g., the receiver function results in Song et al. 2004).  
219 However, theoretically, these two models are identical examined by only triplication data.  
220 Therefore, triplication data alone cannot well constrain a low wave speed zone due to the  
221 tradeoff between the interface depth and the wave speed gradient above it, especially when  
222 we normalize the amplitude by each trace.

## 223 **Array normalization**

224 In most of the previous triplication studies, researchers prefer to normalize the  
225 waveforms by each trace. Normalization is needed because of the uncertainties in the  
226 source magnitude, fault plane solution, attenuation, and station site effects, which make the  
227 absolute amplitudes more difficult to constrain. However, when using the normalized  
228 amplitude of each trace, information about the relative amplitude variations between  
229 stations is lost.

230 In this paper, we propose to use array normalization rather than trace normalization. In  
231 a record section, array normalization means that we normalize all traces relative to one  
232 particular reference station. Because all the records are from the same earthquake, the  
233 source magnitude uncertainty will not affect the results after array normalization.  
234 Furthermore, within the narrow azimuthal range for the particular record section, the effect  
235 of uncertainty in the fault plane solution is also insignificant. When we invert for one  
236 discontinuity, the range of epicenter distances is only within about ten degrees, therefore,

237 we expect the attenuation near the discontinuity within this relatively small range should  
238 not influence the waveforms dramatically. Nevertheless, suppose we have observed  
239 stations with unusual amplitudes either due to attenuation or site effects, we could use trace  
240 normalization for these stations or reduce the weights of them in waveform misfit  
241 contribution for full-waveform inversion.

242 We first compare the trace normalization and array normalization for the two models  
243 shown before (Fig. 2a). In the array-normalized waveforms (Fig. 3a) where amplitude  
244 information between stations is kept, we do observe differences in amplitude between these  
245 two models (the shaded grey region in Fig. 3a). More specifically, the amplitude of the OB  
246 branch for the blue one is smaller than the red one, although still larger than the IASP91  
247 model. Besides, the amplitude for the OD branch is also different. When we apply the  
248 traditional trace normalization (Fig. 3b), since the amplitudes of both the OD and OB  
249 branches are magnified for the blue one, there are no obvious differences between the  
250 waveforms for these two model types (blue and red). In other words, the larger amplitude  
251 of the OB branch comes from the magnification of the trace normalization due to the  
252 smaller amplitude of the OD branch. Therefore, relative amplitude information between  
253 stations in the array-normalized record section (Fig. 3a) can help to distinguish these two  
254 types of models, whose waveforms are almost identical in the traditional trace-normalized  
255 record section (Fig. 3b).

256 We show another comparison between trace normalization and array normalization to  
257 illustrate the necessity of applying array normalization. As shown in Fig. 4c and Fig. 4d,  
258 we present model IASP91 (black) and another designed model (red) with a  $-0.4$  km/s low  
259 wave speed layer only in the shallow part ( $< 150$  km). As shown in Fig. 4a, the array-

260 normalized seismography demonstrates that the different structures in the shallow part will  
261 cause an overall time delay (of  $\sim 3$  s) and affect the amplitude of the direct wave at  
262 different epicentral distances (AO). In comparison, the amplitudes of the later phases (CO)  
263 remain basically unchanged. However, for trace normalization, because the amplitude for  
264 the direct wave (AO) is always the largest within the epicentral distance range before  $15^\circ$ ,  
265 the amplitude of the direct wave is always unity after trace normalization (Fig. 4b).  
266 Therefore, the amplitude of the later phases (CO), which is originally unchanged, seems to  
267 have a smaller amplitude relative to the IASP91 synthetics after the trace normalization.  
268 We note that the later phases (CO) correspond to the reflected wave at the 410-km  
269 discontinuity and the transmitted wave below it. Therefore, the deeper structure is likely to  
270 be incorrectly inverted due to trace normalization (Fig. 4d).

271 As such, besides losing the relative waveform amplitude information between stations  
272 (increasing tradeoff), trace normalization will also lead to the erroneous mapping of the  
273 corresponding structure due to the artificially created mismatch in the waveforms.  
274 Therefore, we propose and recommend using the array-normalization approach for full-  
275 waveform inversion.

## 276 **Synthetic inversion test**

277 Using array normalization, the tradeoff between the interface's depth and the wave speed  
278 gradient above it can be minimized. Here, we will perform a synthetic inversion test to  
279 show to what extent this tradeoff will be reduced and how much of it remains.

280 To obtain quantitative error bounds and avoid the risk of falling into the local minima  
281 faced by the gradient-based inversion method, we adopt the niching genetic algorithm

282 (Koper et al. 1999; Li et al. 2012; Li et al. 2021) in the inversion framework of triplicated  
283 waveforms. Niching genetic algorithm (NGA) is a non-gradient-based inversion scheme  
284 that searches the model space through massive forward modeling and is independent of the  
285 initial model. Only the search range of the model space is given a priori. Moreover,  
286 because NGA involves numerous samplings in the model space, it can provide a series of  
287 acceptable model sets. The mean and variance of these acceptable models can help estimate  
288 the uncertainty of the final model.

289 We design a P-wave synthetic test and apply the array normalization. In this test, we set  
290 model IASP91 as the "ground truth", and invert for the 1-D wave speed profiles using its  
291 corresponding synthetic displacement waveforms as inputs. We set the maximum  
292 epicentral distance to be  $21^\circ$  because within this range the triplicated OB branch is visible.  
293 In the inversion setup, considering the ray path's penetration depths, we only invert the  
294 structure between 210 km and 570 km depths. Within this depth range, we parameterize  
295 the seismic structure with ten unknowns to be inverted. Three parameters are used to  
296 capture the sharp wave speed gradient across the '410-km' discontinuity: two of them are  
297 used to describe the wave speed jump across the discontinuity, the third one represents the  
298 discontinuity depth perturbation. Seven more parameters are set above and below the  
299 interface with a depth interval of  $\sim 40$  km to capture more gradual wave speed changes  
300 away from the discontinuity, we only invert the wave speed at these points. Between two  
301 adjacent anchor points, the wave speeds are linearly interpolated. Beyond this depth range,  
302 the wave speeds are the same as for model IASP91. The P wave speed at each anchor point  
303 is allowed to vary between plus and minus 0.3 km/s, and the position of the discontinuity  
304 varies within plus or minus 20 km, relative to model IASP91 (Fig. 5a). The P wave speed

305 is the only unknown parameter for each anchor point, and the Poisson's ratio and density  
 306 are the same as those in the model IASP91. The effect of attenuation for the P wave is  
 307 considered by applying a constant  $t^*$  value of 1s (Stein & Wysession 2009).

308 As for the misfit window, we choose a continuous one from 32 s to 52 s (reduced time)  
 309 which contains the entire triplicated P wave train, for the case without noise. Before the  
 310 calculation of the misfit, we first cross-correlate the synthetic and observed waveforms for  
 311 the  $i$ th station to obtain the time difference  $\Delta t_i$ . After shifting the synthetic trace by  $\Delta t_i$ ,  
 312 we calculate the L2 norm of the differences between the observed and aligned synthetic  
 313 waveform in the time domain as the misfit function  $\chi_{L2}$ :

$$314 \quad \chi_{L2} = \sum_{i=1}^N \int_{t_1}^{t_2} \left| \frac{\mathbf{d}(\mathbf{x}_i, t)}{\max_{t_1 \leq t \leq t_2} |\mathbf{d}(\mathbf{x}_{ref}, t)|} - \frac{\mathbf{u}(\mathbf{x}_i, t + \Delta t_i)}{\max_{t_1 \leq t \leq t_2} |\mathbf{u}(\mathbf{x}_{ref}, t + \Delta t_{ref})|} \right|^2 dt,$$

315

316 Where  $\mathbf{d}(\mathbf{x}_i, t)$  is the displacement data recorded by the  $i$ th station,  $\mathbf{u}(\mathbf{x}_i, t + \Delta t_i)$  is the  
 317 synthetic data for the  $i$ th station after a time shift of  $\Delta t_i$ . The start and end time for the  
 318 misfit window are  $t_1$  and  $t_2$ , respectively, and  $N$  is the total number of stations used in the  
 319 inversion. The data and synthetics for the reference station are represented by  $\mathbf{d}(\mathbf{x}_{ref}, t)$   
 320 and  $\mathbf{u}(\mathbf{x}_{ref}, t + \Delta t_{ref})$ , respectively, and their maximum absolute values are used for the  
 321 array normalization. This method is highly efficient and converges very quickly. After the  
 322 first 20 generations (100 simulations per generation), the misfit significantly reduces, and  
 323 after 80 generations the misfit starts to converge (Fig. 5c). From the 100 models in the last  
 324 generation, we define the acceptable model with a misfit of less than 10% increase than the  
 325 misfit of the best model. In case, sometimes, the misfit does not readily detect the mismatch,



326 we further examine all the acceptable models by visually comparing the data and synthetics,  
327 to determine the final acceptable candidates.

328 Finally, we have three acceptable model groups (Fig. 5a). The first groups converge to  
329 the ground truth model, verifying the effectiveness of our triplication inversion package.  
330 The other two model groups (group 2 and group 3) are similar to the pair of models we  
331 discussed previously (Fig. 2a). We further use the averaged value of these two groups of  
332 models to calculate their corresponding displacement waveforms. Waveforms between  
333 these two groups are almost identical, and both of them are also quite similar to model  
334 IASP91 waveforms (Fig. 5b).

335 This synthetic test shows that even if the array normalization is applied, this tradeoff  
336 between the interface depth and the wave speed gradient above it cannot be eliminated.  
337 The reason is that a depressed interface truly has a similar impact on the amplitude of the  
338 OB branch compared with a negative wave speed gradient above the interface (Fig. 2c and  
339 2d). Some differences between these two models in the waveforms are less obvious  
340 compared with the travel time curves (Fig. 2b) due to the finite frequency effect.

341 Nevertheless, for a given frequency band, we can estimate the depth uncertainty due to  
342 this tradeoff. These depth limits can be quickly found using this automatic inversion  
343 program. For this case, given this frequency band (half duration of  $\sim 2$  s) and misfit  
344 tolerance, the tradeoff from the wave speed above the discontinuity will lead to a  $\sim 10$  km  
345 uncertainty in the depth estimation.

## 346 **Discontinuity depth and wave speed in the MTZ**

347 In the western Pacific subduction zone, tomography results (Huang & Zhao 2006; Chen  
348 & Pei 2010) indicate a ‘flat slab’ in the MTZ, which increases the wave speeds in the MTZ.  
349 We first test the triplication’s sensitivity to the high wave speed perturbations in the MTZ.  
350 Here we calculated the travel time curves when the wave speed below the 410-km  
351 discontinuity is increased by 0.1 km/s (Fig. 6a) relative to model IASP91, using the Taup  
352 toolkit (Crotwell et al. 1999). Travel time curves show that the wave speed in the MTZ  
353 significantly impacts the CD branch’s travel time (Fig. 6c). In other words, the increase of  
354 the wave speed below the discontinuity will make the transmitted waves (CD) travel faster.  
355 Crossover point (O) marks the intersection of the AB and CD branch, where the waveform  
356 amplitude reaches its maximum. Therefore it is one of the most obvious signatures of this  
357 triplication. In this case, the earlier arrivals of the CD branch will cause the crossover point  
358 (O) to appear at a smaller epicentral distance.

359 Similar behavior of the travel time curves occurs when the depth of the interface is  
360 shallower, and near the subducting slab, the 410-km discontinuity can be elevated due to  
361 the positive Clapeyron slope (e.g., Bina & Helffrich 1994; Flanagan & Shearer 1998).  
362 Assuming a situation where the 410-km discontinuity has a 30-km uplift (Fig. 6b), the CD  
363 branch arrives earlier, and consequently, the crossover point (O) occurs at a smaller  
364 distance (Fig. 6d). This is because, in this situation, this elevated interface is equivalent to  
365 a high wave speed anomaly between 380 km and 410 km depth.

366 It is critical to have stations with smaller epicentral distances (before the crossover point)  
367 to distinguish the model with uplifted discontinuity and the one with high wave speed

368 within MTZ. One difference between these two models (Fig. 6a and 6b) is that when the  
369 410-km discontinuity is uplifted, the earlier arrival of the CD branch can be seen at smaller  
370 epicentral distances where this branch just emerges (cusp C in Fig. 6d and Fig. 6f). While  
371 for the other case where a high wave speed exits in the MTZ, the advance of the CD branch  
372 is not obvious until at epicentral distances greater than the crossover distance (O in Fig. 6c  
373 and 6e).

374 However, stations close to the epicenter near the subduction zone are often scarce which  
375 makes it difficult to distinguish between these two models. Nevertheless, the additional  
376 detailed waveform differences may help differentiate these two models. For example, in  
377 the case of a more considerable wave speed jump beneath the discontinuity, the amplitude  
378 near cusp B remains unchanged (the shaded grey area in Fig. 6e). Meanwhile, for the model  
379 with an uplifted 410-km discontinuity, the amplitude near cusp B is smaller (the shaded  
380 grey area in Fig. 6f). Therefore, even if the travel time differences between the OB and OD  
381 branches are almost identical for these two situations (Fig. 6c and 6d), we can make an  
382 unambiguous distinction between them based on the waveform details at certain epicentral  
383 distances (Fig. 6e and 6f).

## 384 **Application to the Kuril subduction zone**

385 We focus on an intermediate depth (114 km) event that occurred in the Kuril subduction  
386 zone on October 10, 2009, with an  $M_w$  of  $\sim 5.9$  (Fig. 7b). We choose this relatively deep  
387 event to avoid the interference of the depth phases in the triplicated waveforms. The  
388 observed waveforms are selected from a subset of the broadband CEArray stations (Zheng

389 et al. 2010) and the NECESSArray (the NorthEast China Extended SeiSmic Array) in  
390 northeast China. We choose the P-wave data to achieve a better resolution of the MTZ  
391 structure because the P wave is typically observed at a higher frequency than the S wave  
392 due to its smaller attenuation. Therefore, even though the wave speed of the P wave is  
393 larger than that of the S wave, the P wave still has a smaller Fresnel zone. After removing  
394 the instrument response, we have applied a first-order, zero-phase shift Butterworth filter  
395 with a frequency band of 0.05-1 Hz to the data. We choose this relatively broad frequency  
396 band to avoid waveform distortion due to narrow-band filtering. We further divide the  
397 stations into two sublinear arrays according to their azimuthal angles ( $282.5^\circ$  for the  
398 northern region along with ON and  $279.5^\circ$  for the southern region along with OS) and the  
399 observed distinct waveform patterns (Fig. 7e and Fig 7h). Within each sublinear array, the  
400 azimuth range is relatively narrow ( $\sim 1^\circ$ ), and one model should explain all the waveforms  
401 in this particular record section.

402 Compared with the synthetic waveforms shown before (e.g., Fig. 5b), the observed data  
403 are more complex because there are two triplications in each record section. Specifically,  
404 there is a third phase (along the red line in Fig. 7e and Fig. 7h) between the first (the green  
405 line) and the last phase (the black line). This extra phase requires, in the inverted models,  
406 another discontinuity (high-wave speed gradient) below the 410-km discontinuity. By  
407 parameterizing two interfaces in the inversion, we obtain acceptable models indicated by  
408 the shaded red region in Fig. 7f and 7i. We choose one of them to generate the synthetic  
409 waveforms, which show good agreement with the observed waveforms in terms of both  
410 the relative waveform timing and amplitudes on each trace and the relative amplitude  
411 variations between stations (Fig. 7e and Fig. 7h).

412 Certain a priori information is assumed in the inversion. First, given the fact that with  
413 this triplication data alone we cannot exclusively verify the presence of a low wave speed  
414 zone above the 410-km discontinuity, therefore we force the wave speed gradient above  
415 the 410-km discontinuity to be no less than the value in model IASP91. As such, we can  
416 reduce the model unknowns and focus more on inverting the parameters pertaining to the  
417 secondary discontinuity. But we know that given the shortest period of 2 s, a negative wave  
418 speed gradient above the discontinuity can introduce a topographic uplift of  $\sim 10$  km for  
419 the 410-km discontinuity in an equivalently accepted model (Fig. 5a). Second, we set all  
420 the interfaces as a sharp discontinuity to further reduce the number of model unknowns in  
421 the inversion. We will systematically test the sharpness of the discontinuities in the  
422 discussion.

423 Results show that the average depth for the first discontinuity is 420 km and 425 km for  
424 the northern and southern regions, respectively (Fig. 7f and Fig. 7i). The depth uncertainty  
425 is estimated to be  $\sim \pm 5$  km from all the acceptable models given the frequency band of (2  
426 s – 20s). We note that this uncertainty is based on our a priori assumptions. If we fully  
427 consider the tradeoff between different model parameters, another  $\pm 10$ -km uncertainty  
428 should be taken into account. Therefore, the overall estimated depth should be  $420 \pm 15$  km  
429 and  $425 \pm 15$  km for the northern and southern regions, respectively. Turning points, i.e.,  
430 the most sensitive regions of the triplicated wave paths, are below the Tatar Strait of Russia.  
431 Our inverted 410-km discontinuity depths at  $425 \pm 15$  km and  $420 \pm 15$  km are consistent  
432 with the insignificantly uplifted 410-km discontinuity in this region derived from ScS  
433 reverberations (Wang et al. 2017). Furthermore, our result has improved resolution due to  
434 the smaller Fresnel zone of the P wave at a higher frequency ( $\sim 0.5$  Hz).

435 For the secondary discontinuity, it is located at  $490\pm 10$  km and  $475\pm 15$  km for the  
436 northern and southern regions, respectively (Fig. 7f and 7i). The second discontinuity is  
437 located at depths between +1% and +2% wave speed contours (Fig. 7a and 7c) of the  
438 regional FWI model FWEA18 (Tao et al. 2018). We also note that the tradeoff between  
439 the interface depth and the wave speed gradient above it can be observed from the  
440 acceptable models. In this region, the upper slab surface is located  $\sim 50$ -70 km below the  
441 410-km discontinuity (Fig. 7f and 7i). The cooling effect from this relatively distant slab  
442 should be weak, which also explains the insignificant uplift of the 410-km discontinuity.

## 443 **Discussion**

### 444 **Comparison with the 3-D regional FWI model**

445 Tomographic velocity model FWEA18 (Tao et al. 2018) is the currently highest  
446 resolution FWI model in this region. Because FWEA18 is inverted with body waves with  
447 the shortest period of 8 s, thus it is important to examine how well this model can predict  
448 the body waves of a higher frequency of 2 s and if further refinement of the model is  
449 necessary. Due to the prohibitive computational cost of 3-D simulations for 2-s waves, 2-  
450 D simulations are performed for the profiles close to the selected stations which are  
451 sublinear. The 2-D models along with profiles ON and OS (Fig. 7a and 7c) are extracted  
452 from 3-D model FWEA18 and implemented in the 2-D finite-difference (FD) package (Li  
453 et al. 2014) to generate the 2-D synthetics. This 2-D package has incorporated several  
454 corrections, e.g., out-of-plane spreading, point source excitation, and Earth-flattening, to  
455 better account for the 3-D wavefield spreading (Li et al. 2014).

456       Waveform fitting comparison indicates that although the model FWEA18 predicts the  
457 observed 2-s waveforms much better (Fig. 7d and Fig. 7g) than the model IASP91 (Fig.  
458 S1a and S1b), its synthetics still can't fit the data completely. The mismatch mainly comes  
459 from the differential travel time between the direct wave and the refracted wave, which is  
460 smaller in the FWEA18 synthetics (Fig. 7d and 7g) than in the data (the black and green  
461 lines in Fig. 7e and Fig. 7h). This mismatch suggests that although the high P wave speed  
462 perturbation within the slab of model FWEA18 is very strong, twice the perturbation within  
463 the slab of model GAP-P4 (Obayashi et al. 2013), the perturbation is still not large enough  
464 to advance the refracted phases relative to the direct waves. The underestimation of wave  
465 speed perturbation within the slab model FWEA18 is likely caused by the relatively long  
466 period data ( $> 8$  s) used in the model inversion. Through the 1-D full-waveform inversion  
467 in this study, we can find acceptable models with adequate wave speed jump across the  
468 slab upper surface. More significantly, these models can predict not only the differential  
469 travel time between the direct and the refracted waves but also an additional move-out in  
470 the record sections (indicated by the red line in Fig. 6e and 6h). Therefore, 1-D full-  
471 waveform inversion based on a higher frequency ( $\sim 2$  s) waveforms is indispensable to  
472 reveal precise structures such as the wave speed jump across the slab upper surface, which  
473 will be discussed in the following subsections.

474       For all the stations in the northern region, both the data and synthetics are normalized  
475 according to station WDL so that the relative amplitudes between stations are preserved.  
476 We also observe a large amplitude difference between the data and the FWEA18 synthetics  
477 for station XUK, but a much smaller amplitude difference between data and the synthetics  
478 of the model inverted in this study. This large amplitude discrepancy between data and

479 FWEA18 synthetics can be explained by the misfit function used in the inversion, which  
480 is based on normalized-zero-lag cross-correlation (Tao et al. 2017) and insensitive to the  
481 amplitude differences. This suggests that full-waveform inversion with preserved relative  
482 waveform amplitude is necessary to recover more realistic models that can predict the  
483 waveform data across the array.

## 484 **Discontinuity sharpness**

485 The discontinuity sharpness is one of the critical parameters to distinguish models with  
486 mineralogical phase changes and chemical layering (Benz & Vidale 1993). In addition, the  
487 sharpness of the 410-km discontinuity is sensitive to the water content (Helffrich & Wood  
488 1996) and is critical to understand the deep water cycle of the Earth (Thompson 1992).

489 In our inversions, to reduce the model unknowns, we set all the discontinuities as sharp  
490 interfaces. However, it is important to discuss if the 2-s waveforms in this study can resolve  
491 the sharpness across the 410-km discontinuity and the slab upper surface. The systematic  
492 waveform modeling tests with different 410-km discontinuity thickness (0 km, 20 km, and  
493 40 km as shown in Fig. S2a) show that the discontinuity thickness has the biggest impact  
494 on the extent of the BC branch, with thicker discontinuity corresponding to a smaller extent  
495 on the travel time curve (Fig. S2b). In these tests, we keep the wave speeds the same above  
496 and below the 410-km transitional zone as model IASP91, but only vary the thickness  
497 centered at the depth of 410 km.

498 However, different from the impact of the discontinuity thickness on the travel time  
499 curves calculated based on ray theory, the corresponding 3-s waveforms of the BC branch



500 exhibit no sensitivity to the discontinuity thickness even up to 40 km (Fig. S2c), which is  
501 likely due to the wavefront healing, a finite frequency effect (Nolet & Dahlen 2000).

502 We perform a set of forward modeling tests to further investigate the sensitivity of  
503 waveforms with different dominant frequency periods (3 s, 2 s, and 1 s) to the discontinuity  
504 thickness up to 40 km (Fig. S2c-e). As the frequency increases (e.g., from 2 s to 1 s), the  
505 waveform differences become more apparent between the sharper and gradual  
506 discontinuities, especially for the pre-critical reflections at a smaller epicentral distance  
507 (Fig. S2d and S2e). A similar frequency-dependent sensitivity to the discontinuity  
508 thickness has also been observed in previous triplication studies (Melbourne & Helmberger  
509 1998; Zhang et al. 2019). Given the fact that 2-s waveforms cannot discern a model with a  
510 sharp jump across the 410-km discontinuity from the model with a certain thickness.  
511 Therefore, in the inversion, we set the discontinuity as a sharp interface. Nevertheless, the  
512 inverted sharp interface's depth should reflect the center of alternative gradual interfaces  
513 with a certain thickness.

514 To investigate the sharpness of the slab upper surface, we apply waveform inversion to  
515 the real data. In the southern region, we fix the midpoint of the interface at 480 km and set  
516 its thickness to be 20 km, 40 km, 60 km, 80 km (Fig. S3a). For each interface thickness,  
517 the full-waveform inversion is performed to search for the acceptable models. Up to 60 km  
518 for the slab upper interface thickness, the models inverted can predict the second  
519 triplication on the observed waveform (annotated by the black arrow in Fig. S3b). However,  
520 when the thickness reaches 80 km, the wave speed gradient is too small to generate the  
521 second triplication. Therefore, triplication waveforms of 2 s alone, recorded from one event,  
522 are unable to discern the slab interface thickness between 0 km and 60 km, but they

523 certainly require the thickness to be less than 80 km. There is also a challenge to use shorter  
524 period waveforms from lower magnitude earthquakes, due to the low signal-to-noise ratio.  
525 Nevertheless, combining triplication data with converted or underside reflected phases  
526 could better constrain the discontinuity's sharpness in the future. Additionally, for the  
527 accepted model with a slab interface thickness of 60 km, the positive wave speed gradient  
528 within the inverted slab is twice the average value of model FWEA18, which will be further  
529 discussed in the next section.

### 530 **Wave speed jumps across the slab upper surface**

531 Although the model FWEA18 shows a 2-D structure, in the cross-section roughly  
532 parallel to the strike direction of the slab, its structure near the turning points of the wave  
533 paths varies little laterally and can be treated as a 1-D layered model (the grey region in  
534 Fig. 7a and 7c) with averaged velocity from the epicentral distance of  $5^\circ$  to  $14^\circ$  (dashed  
535 black lines in Fig. 7f and 7i). To obtain the wave speed jump across the slab interface, we  
536 choose the wave speed values at points 30 km (on the order of one wavelength of the  
537 waveform) above and below the inverted interface for both the averaged model of the  
538 inverted acceptable models and model FWEA18. This helps avoid the complication due to  
539 the tradeoff between the interface depth and the wave speed in its vicinity. We also isolate  
540 the wave speed jump due to the cold slab both in the inverted models and model FWEA18  
541 by removing 0.2 km/s waves speed jump due to pressure and temperature increase in the  
542 ambient mantle in the vicinity of the slab interface.

543 The inverted wave speed jump across the slab upper surface is  $\sim 3.9\%$  and  $\sim 4.6\%$  for  
544 the northern and southern regions, respectively. These wave speed jumps are about twice

545 the values from the averaged FWEA18 model, i.e.,  $\sim 2.0\%$  and  $\sim 2.4\%$  for the northern  
546 and southern regions, respectively. The 2.0% to 2.4% wave speed perturbations for the slab  
547 can neither fit the relative timing nor produce the extra triplicated phase observed in the  
548 data, therefore can be treated as the minimum limit value for the subducting slab in this  
549 region. As for the 3.9% to 4.6% wave speed jump from our inverted results, they are  
550 robustly constrained and not affected much by the slab interface thickness, e.g., a sharp  
551 interface and a 60-km thick interface (Fig. S3a). Nevertheless, our inverted wave speed  
552 jump of 3.9% to 4.6% can be viewed as the maximum limit value, because these values  
553 can be overestimated when the source region slab perturbations are not accounted for.  
554 Therefore, the wave speed jump across the slab upper surface over a depth range of 60 km  
555 should be between 2.4% and 4.6%. This relatively larger wave speed perturbation of the slab  
556 is consistent with the fast core ( $\sim 5\%$ ) discovered in the same Kuril subduction zone by  
557 modeling the teleseismic waveforms recorded in the down-dip direction (Zhan et al. 2014).

## 558 **Future improvement**

559 Because triplications are most sensitive to the turning points of the wave paths, we only  
560 inverted for the structures in the deeper region where there are enough path crossings.  
561 However, the effect of shallow structures should be considered. Although triplication can  
562 minimize the influence from the shallower structure due to the similar wave paths in the  
563 shallower part (e.g., Li et al. 2021), when the unconstrained structure is close to the depth  
564 range to be inverted, the triplicated waveforms can still be influenced (Fig. 4a). To  
565 overcome this, the shallow part needs to be pre-constrained with a priori information from  
566 independent studies (e.g., Chu & Helmberger 2014). In this study, for the region above 300

567 km, we use the value from the averaged model FWEA18 to minimize the influence from  
568 the shallower structure. Our inverted wave speeds are consistent with the averaged values  
569 of the model FWEA18 even down to 360 km (Fig. 7f and 7i), which confirms that choosing  
570 the pre-constrained model to the depth of 300 km is reasonable.

571 Strong lateral heterogeneities can also influence the full-waveform inversion results  
572 based on 1-D assumptions. Previous studies indicate that 2-D and 3-D slab structures near  
573 the wave path turning points can affect the triplicated waveforms (e.g., Wang et al. 2014  
574 and Tao et al. 2017). To minimize such influence from lateral heterogeneities, we  
575 purposefully choose the event-station configuration with wave paths roughly parallel to the  
576 slab's depth contours where the slab structure can be approximated as 1-D near the turning  
577 points (Fig. 7a and 7c). However, near the earthquake source, the high wave speed slab is  
578 roughly parallel to the ray paths. This accumulated effect of the source-side wave speed  
579 perturbation along the ray paths cannot be neglected (Li et al. 2016). Otherwise, the slab  
580 wave speed perturbation near the wave path turning points can be overestimated and our  
581 inverted wave speed jump of 3.9% to 4.6% can only be viewed as the upper bound. To  
582 overcome the limitation of not accounting for the source region heterogeneity, the 2-D FD  
583 method can be implemented in the future to replace the current 1-D simulation tool QSEIS,  
584 which can take into account the lateral heterogeneities either in the shallower part or near  
585 the source side with a priori information, e.g., tomography results from other studies. To  
586 reduce the vast computational costs, the GPU version of the 2-D FD method (Li et al. 2014)  
587 can be utilized. The current non-gradient-based framework still works with the fast speed  
588 of the GPU-based 2-D FD simulations, although it is beyond the scope of this study.

589 We note that this work is a case study showing the effectiveness of the high-frequency  
590 ( $\sim 2$  s) triplications in resolving MTZ discontinuities and the slab upper surface. More  
591 events and stations are needed to better constrain the model because the full-waveform  
592 inversion results in this study strongly depend on the details of high-quality waveforms.  
593 Take the northern region as an example, if we consider another model with a low wave  
594 speed zone between the 410-km discontinuity and the slab upper surface (Fig. S4c), the  
595 waveform fitting is similar but slightly different (Fig. S4a and S4d) from the model without  
596 this zone (Fig. S4b). Due to the limited number of stations, the details of the waveform  
597 cannot be verified as consistent and robust waveform features or subjected to noise  
598 contamination. To definitively discriminate these two models, more high-quality  
599 waveforms with better spatial coverage are required not only for 1-D full-waveform  
600 inversion but also for obtaining a 3-D model of discontinuity structure in this region (e.g.,  
601 Stahler et al. 2012; Takeuchi et al. 2014).

## 602 **Conclusions**

603 Triplicated body waves effectively sample the structure near the transition zone and  
604 carry rich information of the discontinuities regarding their depths and wave speed  
605 gradients. The 1-D non-gradient-based full-waveform inversion (FWI) of triplication  
606 waveforms is a useful and efficient tool in accurately mapping the MTZ structural details  
607 to the first order from the high-frequency waveforms.

608 We systematically analyzed the tradeoff between the depth of the discontinuity and the  
609 low wave speed gradient above it, discussed the necessity of using array normalized

610 amplitude, and applied the 1-D FWI method in inverting the 1-D structure below the Tatar  
611 Strait of Russia.

612 We observe triplications due to both the 410-km discontinuity and the slab upper surface,  
613 the seismic structures of which are simultaneously inverted. Our derived 410-km  
614 discontinuity depths are at  $420 \pm 15$  km and  $425 \pm 15$  km, with no observable uplift. The  
615 average depth of the slab upper surface is inverted to be located about 50-70 km below the  
616 410-km discontinuity, between the 1%-2% wave speed contour of the regional tomography  
617 results (Tao et al. 2018), but we find twice the amplitude of the wave speed perturbation.  
618 A strong wave speed jump between 2.4% and 4.6% (potentially over a depth range of 60  
619 km) is critically necessary to both fit the differential travel time between main phases and  
620 generate an extra triplication phase observed in the data. Our inverted wave speed jump  
621 across the slab upper surface is consistent with the strong wave speed perturbation of ~5%  
622 in the cold slab core (Zhan et al. 2014) as well as the results from the residual sphere  
623 method (Ding & Grand 1994) in the same region. Our study also indicates that full-  
624 waveform inversion at a relatively higher frequency band (~ 2s) is required to resolve the  
625 detailed and precise structures near the MTZ. Due to the prohibitive computational cost  
626 with 3-D full-waveform inversion, the method used in this study provide an incremental  
627 yet effective approach to probe the MTZ structure perturbed by the subducting slabs.

## 628 **Acknowledgments**

629 Seismic records used in this study came from the CEArray and the NECESSArray, and  
630 we thank the team members for their deployments. We thank Editor Ebru Bozdog, reviewer  
631 Maria Koroni, and another anonymous reviewer for their constructive suggestions. We

632 thank Chunquan Yu for helping with the 2-D simulation and Kao Tao, Shawn S. Wei,  
633 Mingda Lv, Xiaobo He, Chen Cai, Ziyi Xi, and Zhigang Peng for valuable discussion. We  
634 acknowledge the course "English Composition for Geophysical Research" by Li Zhao of  
635 Peking University for help in improving this manuscript. We thank the IRIS Data  
636 Management Center for the access to waveforms used in the focal depth inversion. We  
637 thank the Institute for Cyber-Enabled Research (ICER) at Michigan State University, the  
638 Extreme Science and Engineering Discovery Environment (XSEDE supported by NSF  
639 grant ACI-1053575), and the High-performance Computing Platform of Peking University  
640 for providing the high-performance computing resources. The map-view figure is produced  
641 using the GMT software of (Wessel & Smith 1998). This research was supported by NSF  
642 grant 1802247 and the startup fund of Min Chen at Michigan State University.

643

644

645

646

647

648

649

650

651

652 **References**

- 653 Benz, H. M., & Vidale, J. E. (1993). Sharpness of uppermantle discontinuities determined  
654 from high-frequency reflections. *Nature*, 365(6442), 147-150.
- 655 Bercovici, D., & Karato, S. I. (2003). Whole-mantle convection and the transition-zone  
656 water filter. *Nature*, 425(6953), 39-44.
- 657 Bina, C. R., & Helffrich, G. (1994). Phase transition Clapeyron slopes and transition zone  
658 seismic discontinuity topography. *Journal of Geophysical Research: Solid*  
659 *Earth*, 99(B8), 15853-15860.
- 660 Bozdağ, E., Peter, D., Lefebvre, M., Komatitsch, D., Tromp, J., Hill, J., ... & Pugmire, D.  
661 (2016). Global adjoint tomography: first-generation model. *Geophysical Journal*  
662 *International*, 207(3), 1739-1766.
- 663 Brudzinski, M. R., & Chen, W. P. (2000). Variations in P wave speeds and outboard  
664 earthquakes: evidence for a petrologic anomaly in the mantle transition  
665 zone. *Journal of Geophysical Research: Solid Earth*, 105(B9), 21661-21682.
- 666 Chapman, C. H. (1978). A new method for computing synthetic  
667 seismograms. *Geophysical Journal International*, 54(3), 481-518.
- 668 Chen, Y. J., & Pei, S. (2010). Tomographic structure of East Asia: II. Stagnant slab above  
669 660 km discontinuity and its geodynamic implications. *Earthquake Science*, 23(6),  
670 613-626.
- 671 Chevrot, S., Vinnik, L., & Montagner, J. P. (1999). Global-scale analysis of the mantle  
672 Pds phases. *Journal of Geophysical Research: Solid Earth*, 104(B9), 20203-20219.
- 673 Chu, R., & Helmberger, D. (2014). Lithospheric waveguide beneath the Midwestern  
674 United States; massive low - velocity zone in the lower crust. *Geochemistry,*  
675 *Geophysics, Geosystems*, 15(4), 1348-1362.
- 676 Chu, R., Schmandt, B., & Helmberger, D. V. (2012). Upper mantle P velocity structure  
677 beneath the Midwestern United States derived from triplicated  
678 waveforms. *Geochemistry, Geophysics, Geosystems*, 13(2).
- 679 Collier, J. D., & Helffrich, G. R. (1997). Topography of the “410” and “660” km seismic  
680 discontinuities in the Izu-Bonin subduction zone. *Geophysical research*  
681 *letters*, 24(12), 1535-1538.



- 682 Crotwell, H. P., Owens, T. J., & Ritsema, J. (1999). The TauP Toolkit: Flexible seismic  
683 travel-time and ray-path utilities. *Seismological Research Letters*, 70(2), 154-160.
- 684 Ding, X. Y., & Grand, S. P. (1994). Seismic structure of the deep Kurile subduction  
685 zone. *Journal of Geophysical Research: Solid Earth*, 99(B12), 23767-23786.
- 686 Flanagan, M. P., & Shearer, P. M. (1998). Global mapping of topography on transition  
687 zone velocity discontinuities by stacking SS precursors. *Journal of Geophysical  
688 Research: Solid Earth*, 103(B2), 2673-2692.
- 689 Flanagan, M. P., & Shearer, P. M. (1999). A map of topography on the 410-km  
690 discontinuity from PP precursors. *Geophysical research letters*, 26(5), 549-552.
- 691 Fukao, Y., Widiyantoro, S., & Obayashi, M. (2001). Stagnant slabs in the upper and  
692 lower mantle transition region. *Reviews of Geophysics*, 39(3), 291-323.
- 693 Gao, W., Matzel, E., & Grand, S. P. (2006). Upper mantle seismic structure beneath  
694 eastern Mexico determined from P and S waveform inversion and its  
695 implications. *Journal of Geophysical Research: Solid Earth*, 111(B8).
- 696 Grand, S. P., & Helmberger, D. V. (1984). Upper mantle shear structure of North  
697 America. *Geophysical Journal International*, 76(2), 399-438.
- 698 Green II, H. W., & Burnley, P. C. (1989). A new self-organizing mechanism for deep-  
699 focus earthquakes. *Nature*, 341(6244), 733-737.
- 700 Gu, Y. J., & Dziewonski, A. M. (2002). Global variability of transition zone  
701 thickness. *Journal of Geophysical Research: Solid Earth*, 107(B7), ESE-2.
- 702 Guo, Z., & Zhou, Y. (2020). Finite-frequency imaging of the global 410-and 660-km  
703 discontinuities using SS precursors. *Geophysical Journal International*, 220(3),  
704 1978-1994.
- 705 Han, G., Li, J., Guo, G., Mooney, W. D., Karato, S. I., & Yuen, D. A. (2021). Pervasive  
706 low-velocity layer atop the 410-km discontinuity beneath the northwest Pacific  
707 subduction zone: Implications for rheology and geodynamics. *Earth and Planetary  
708 Science Letters*, 554, 116642.
- 709 Helffrich, G. R., & Wood, B. J. (1996). 410 km discontinuity sharpness and the form of  
710 the olivine  $\alpha$ - $\beta$  phase diagram: resolution of apparent seismic  
711 contradictions. *Geophysical Journal International*, 126(2), F7-F12.

- 712 Niazi, M., & Anderson, D. L. (1965). Upper mantle structure of western North America  
713 from apparent velocities of P waves. *Journal of Geophysical Research*, 70(18),  
714 4633-4640.
- 715 Houser, C., Masters, G., Flanagan, M., & Shearer, P. (2008). Determination and analysis  
716 of long-wavelength transition zone structure using SS precursors. *Geophysical*  
717 *Journal International*, 174(1), 178-194.
- 718 Huang, J., & Zhao, D. (2006). High-resolution mantle tomography of China and  
719 surrounding regions. *Journal of Geophysical Research: Solid Earth*, 111(B9).
- 720 Isacks, B., & Molnar, P. (1971). Distribution of stresses in the descending lithosphere from  
721 a global survey of focal-  
722 mechanism solutions of mantle earthquakes. *Reviews of Geophysics*, 9(1), 103-174.
- 723 Johnson, L. R. (1967). Array measurements of P velocities in the upper mantle. *Journal*  
724 *of Geophysical Research*, 72(24), 6309-6325.
- 725 Kawakatsu, H., & Watada, S. (2007). Seismic evidence for deep-water transportation in  
726 the mantle. *Science*, 316(5830), 1468-1471.
- 727 Kennett, B. L. N., & Engdahl, E. R. (1991). Traveltimes for global earthquake location  
728 and phase identification. *Geophysical Journal International*, 105(2), 429-465.
- 729 Kirby, S. H., Durham, W. B., & Stern, L. A. (1991). Mantle phase changes and deep-  
730 earthquake faulting in subducting lithosphere. *Science*, 252(5003), 216-225.
- 731 Koper, K. D., Wyession, M. E., & Wiens, D. A. (1999). Multimodal function  
732 optimization with a niching genetic algorithm: A seismological example. *Bulletin of*  
733 *the Seismological Society of America*, 89(4), 978-988.
- 734 Koroni, M., & Trampert, J. (2021). Imaging global mantle discontinuities: a test using  
735 full-waveforms and adjoint kernels. *Geophysical Journal International*.
- 736 Lawrence, J. F., & Shearer, P. M. (2008). Imaging mantle transition zone thickness with  
737 SdS-SS finite-frequency sensitivity kernels. *Geophysical Journal*  
738 *International*, 174(1), 143-158.
- 739 Li, D., Helmberger, D., Clayton, R. W., & Sun, D. (2014). Global synthetic seismograms  
740 using a 2-D finite-difference method. *Geophysical Journal International*, 197(2),  
741 1166-1183.

- 742 Li, G., Bai, L., Zhou, Y., Wang, X., & Cui, Q. (2017). Velocity structure of the mantle  
743 transition zone beneath the southeastern margin of the Tibetan  
744 Plateau. *Tectonophysics*, 721, 349-360.
- 745 Li, G., Li, Y. E., Zhang, H., Bai, L., Ding, L., Li, W., ... & Zhou, Y. (2019). Detection of  
746 a thick and weak low-velocity layer atop the mantle transition zone beneath the  
747 Northeastern South China Sea from triplicated P-wave waveform modeling. *Bulletin  
748 of the Seismological Society of America*, 109(4), 1181-1193.
- 749 Li, J., Chen, M., Koper, K. D., Zhou, T., Xi, Z., Li, S., & Li, G. (2021). FastTrip: A Fast  
750 MPI - Accelerated 1D Triplication Waveform Inversion Package for Constraining  
751 Mantle Transition Zone Discontinuities. *Seismological Research Letters*.
- 752 Li, J., Wang, S., Cai, C., Ning, J. (2016). A Computational Scheme for Quantitatively  
753 Removing the Effects of Lateral Velocity Variation on 1-D Triplicated Wave  
754 Velocity Inversion [J]. *Acta Scientiarum Naturalium Universitatis Pekinensis*, 2016,  
755 52(3): 420-426.
- 756 Li, L., Chen, Y. W., Zheng, Y., Hu, H., & Wu, J. (2019). Seismic evidence for plume-  
757 slab interaction by high-resolution imaging of the 410-km discontinuity under  
758 Tonga. *Geophysical Research Letters*, 46(23), 13687-13694.
- 759 Li, S., Wang, Y., Liang, Z., He, S., & Zeng, W. (2012). Crustal structure in southeastern  
760 Gansu from regional seismic waveform inversion. *Chinese Journal of  
761 Geophysics*, 55(2), 206-218.
- 762 Melbourne, T., & Helmberger, D. (1998). Fine structure of the 410-km  
763 discontinuity. *Journal of Geophysical Research: Solid Earth*, 103(B5), 10091-10102.
- 764 Molnar, P., Freedman, D., & Shih, J. S. (1979). Lengths of intermediate and deep seismic  
765 zones and temperatures in downgoing slabs of lithosphere. *Geophysical Journal Inte  
766 rnational*, 56(1), 41-54.
- 767 Niu, F., Levander, A., Ham, S., & Obayashi, M. (2005). Mapping the subducting Pacific  
768 slab beneath southwest Japan with Hi-net receiver functions. *Earth and Planetary  
769 Science Letters*, 239(1-2), 9-17.
- 770 Nolet, G., & Dahlen, F. A. (2000). Wave front healing and the evolution of seismic delay  
771 times. *Journal of Geophysical Research: Solid Earth*, 105(B8), 19043-19054.
- 772 Revenaugh, J., & Sipkin, S. A. (1994). Seismic evidence for silicate melt atop the 410-  
773 km mantle discontinuity. *Nature*, 369(6480), 474-476.

- 774 Ringwood, A. E. (1975). *Composition and Petrology of the Earth's Mantle*. MacGraw-  
775 Hill, 618.
- 776 Ritsema, J., Cupillard, P., Tauzin, B., Xu, W., Stixrude, L., & Lithgow-Bertelloni,  
777 C. (2009). Joint mineral physics and seismic wave traveltime analysis of upper  
778 mantle temperature. *Geology*, 37(4), 363-366.
- 779 Ritsema, J., Xu, W., Stixrude, L., & Lithgow-Bertelloni, C. (2009). Estimates of the  
780 transition zone temperature in a mechanically mixed upper mantle. *Earth and  
781 Planetary Science Letters*, 277(1-2), 244-252.
- 782 Schmandt, B., Dueker, K. G., Hansen, S. M., Jasbinsek, J. J., & Zhang, Z. (2011). A  
783 sporadic low-velocity layer atop the western US mantle transition zone and short-  
784 wavelength variations in transition zone discontinuities. *Geochemistry, Geophysics,  
785 Geosystems*, 12(8).
- 786 Schmerr, N., & Garnero, E. J. (2007). Upper mantle discontinuity topography from  
787 thermal and chemical heterogeneity. *Science*, 318(5850), 623-626.
- 788 Shearer, P. M. (2000). Upper mantle seismic discontinuities. *GEOPHYSICAL  
789 MONOGRAPH-AMERICAN GEOPHYSICAL UNION*, 117, 115-132.
- 790 Song, T. R. A., Helmberger, D. V., & Grand, S. P. (2004). Low-velocity zone atop the  
791 410-km seismic discontinuity in the northwestern United States. *Nature*, 427(6974),  
792 530-533.
- 793 Stähler, S. C., Sigloch, K., & Nissen-Meyer, T. (2012). Triplicated P-wave measurements  
794 for waveform tomography of the mantle transition zone. *Solid Earth*, 3(2), 339-354.
- 795 Stein, S., & Wysession, M. (2009). *An introduction to seismology, earthquakes, and earth  
796 structure*. John Wiley & Sons.
- 797 Tajima, F., & Grand, S. P. (1995). Evidence of high velocity anomalies in the transition  
798 zone associated with southern Kurile subduction zone. *Geophysical research  
799 letters*, 22(23), 3139-3142.
- 800 Takeuchi, N., Kawakatsu, H., Tanaka, S., Obayashi, M., Chen, Y. J., Ning, J., ... &  
801 Tonegawa, T. (2014). Upper mantle tomography in the northwestern Pacific region  
802 using triplicated P waves. *Journal of Geophysical Research: Solid Earth*, 119(10),  
803 7667-7685.
- 804 Tao, K., Grand, S. P., & Niu, F. (2017). Full-waveform inversion of triplicated data using  
805 a normalized-correlation-coefficient-based misfit function. *Geophysical Journal  
806 International*, 210(3), 1517-1524.

- 807 Tao, K., Grand, S. P., & Niu, F. (2018). Seismic structure of the upper mantle beneath  
808 eastern Asia from full waveform seismic tomography. *Geochemistry, Geophysics,*  
809 *Geosystems*, 19(8), 2732-2763.
- 810 Thiriot, J. L., Montagner, J. P., & Vinnik, L. (1998). Upper-mantle seismic discontinuities  
811 in a subduction zone (Japan) investigated from P to S converted waves. *Physics of*  
812 *the earth and planetary interiors*, 108(1), 61-80.
- 813 Thompson, A. B. (1992). Water in the Earth's upper mantle. *Nature*, 358(6384), 295-302.
- 814 Tian, D., Lv, M., Wei, S. S., Dorfman, S. M., & Shearer, P. M. (2020). Global variations  
815 of Earth's 520-and 560-km discontinuities. *Earth and Planetary Science Letters*, 552,  
816 116600.
- 817 Tromp, J., Tape, C., & Liu, Q. (2005). Seismic tomography, adjoint methods, time revers  
818 al and banana-doughnut kernels. *Geophysical Journal International*, 160(1), 195-  
819 216.
- 820 Van der Meijde, M., Marone, F., Giardini, D., & Van der Lee, S. (2003). Seismic  
821 evidence for water deep in Earth's upper mantle. *Science*, 300(5625), 1556-1558.
- 822 Vidale, J. E., & Benz, H. M. (1992). Upper-  
823 mantle seismic discontinuities and the thermal structure of subduction zones. *Nature*,  
824 356(6371), 678-683.
- 825 Vinnik, L. P. (1977). Detection of waves converted from P to SV in the mantle. *Physics*  
826 *of the Earth and planetary interiors*, 15(1), 39-45.
- 827 Wang, R. (1999). A simple orthonormalization method for stable and efficient  
828 computation of Green's functions. *Bulletin of the Seismological Society of*  
829 *America*, 89(3), 733-741.
- 830 Wang, T., & Chen, L. (2009). Distinct velocity variations around the base of the upper  
831 mantle beneath northeast Asia. *Physics of the Earth and Planetary Interiors*, 172(3-  
832 4), 241-256.
- 833 Wang, T., Revenaugh, J., & Song, X. (2014). Two-dimensional/three-dimensional  
834 waveform modeling of subducting slab and transition zone beneath Northeast  
835 Asia. *Journal of Geophysical Research: Solid Earth*, 119(6), 4766-4786.
- 836 Wang, X., Li, J., & Chen, Q. F. (2017). Topography of the 410 km and 660 km  
837 discontinuities beneath the Japan Sea and adjacent regions by analysis of multiple-  
838 ScS waves. *Journal of Geophysical Research: Solid Earth*, 122(2), 1264-1283.

- 839 Wang, Y., Wen, L., & Weidner, D. (2009). Array triplication data constraining seismic  
840 structure and composition in the mantle. *Surveys in geophysics*, 30(4), 355-376.
- 841 Wei, S. S., & Shearer, P. M. (2017). A sporadic low-velocity layer atop the 410 km  
842 discontinuity beneath the Pacific Ocean. *Journal of Geophysical Research: Solid*  
843 *Earth*, 122(7), 5144-5159.
- 844 Wei, S. S., Shearer, P. M., Lithgow-Bertelloni, C., Stixrude, L., & Tian, D. (2020).  
845 Oceanic plateau of the Hawaiian mantle plume head subducted to the uppermost  
846 lower mantle. *Science*, 370(6519), 983-987.
- 847 Wessel, P., & Smith, W. H. (1998). New, improved version of Generic Mapping Tools  
848 released. *Eos, Transactions American Geophysical Union*, 79(47), 579-579.
- 849 Zhan, Z., Helmberger, D. V., & Li, D. (2014). Imaging subducted slab structure beneath  
850 the Sea of Okhotsk with teleseismic waveforms. *Physics of the Earth and Planetary*  
851 *Interiors*, 232, 30-35.
- 852 Zhang, M., Sun, D., Wang, Y., & Wu, Z. (2019). Fine structure of the 660-km  
853 discontinuity beneath southeastern China. *Geophysical Research Letters*, 46(13),  
854 7304-7314.
- 855 Zheng, X. F., Yao, Z. X., Liang, J. H., & Zheng, J. (2010). The role played and  
856 opportunities provided by IGP DMC of China National Seismic Network in  
857 Wenchuan earthquake disaster relief and researches. *Bulletin of the Seismological*  
858 *Society of America*, 100(5B), 2866-2872.

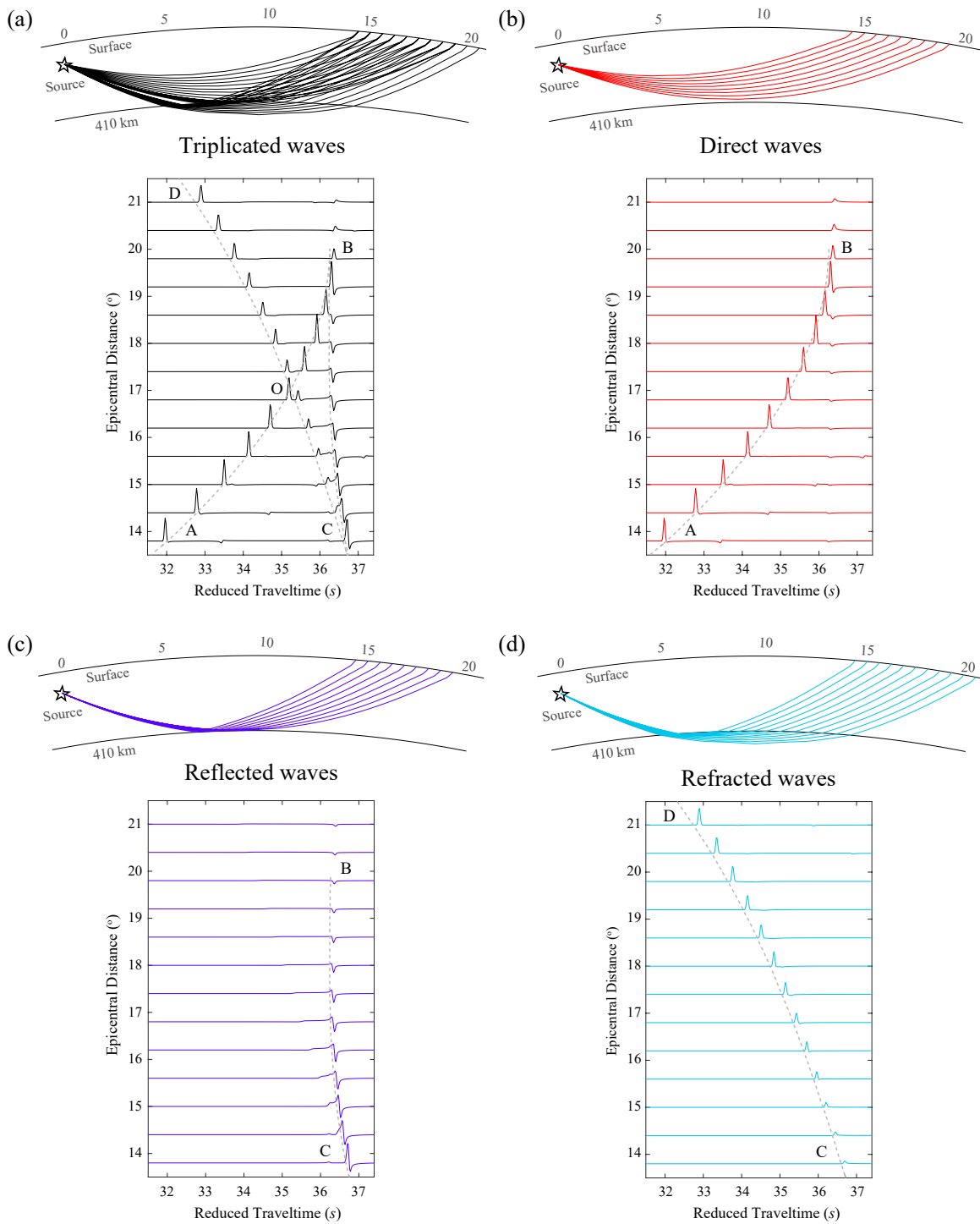


**Figure 1.** Ray paths and waveforms for P-wave triplications. (a) Ray paths and waveforms for all the triplicated P waves. In the upper panel, the black star is the earthquake source at 114 km, and black lines show all the ray paths. In the lower panel, the black waveforms are synthetics, and the dashed grey lines are the travel time curves. AB, BC, and CD branches represent the direct waves, reflected waves, and refracted waves, respectively. The O point shows the crossover point of the AB and BC branch. A reducing slowness of  $11.5 \text{ s}^\circ$  is used. (b) Ray paths and waveforms for the direct waves AB. (c) Ray paths and waveforms for the reflected waves BC. (d) Ray paths and waveforms for the refracted waves CD.

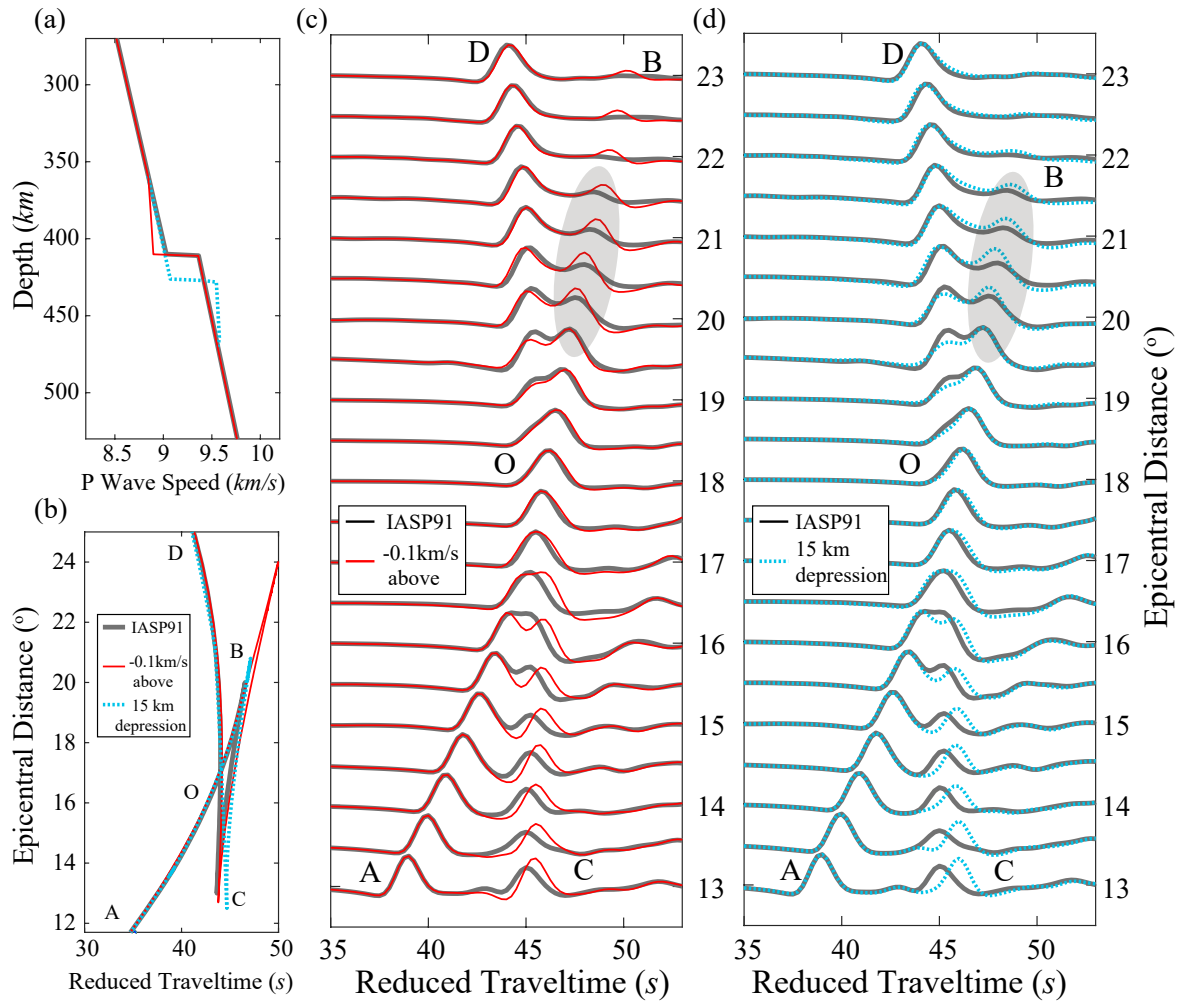


**Figure 2.** Modeling tests for the tradeoff between model parameters. (a) The bold grey line shows the model IASP91, the solid red line indicates the model with a low wave speed zone above the discontinuity, and the dashed blue line represents the model with a 15-km depression for the interface. (b) Travel time curves for the models in (a) with the same line styles. (c) Waveform comparison between the model IASP91 (grey) and the solid red model in (a). (d) Waveform comparison between the model IASP91 and the dashed blue model in (a). The amplitude is normalized by each trace and waveforms in the grey region are similar.



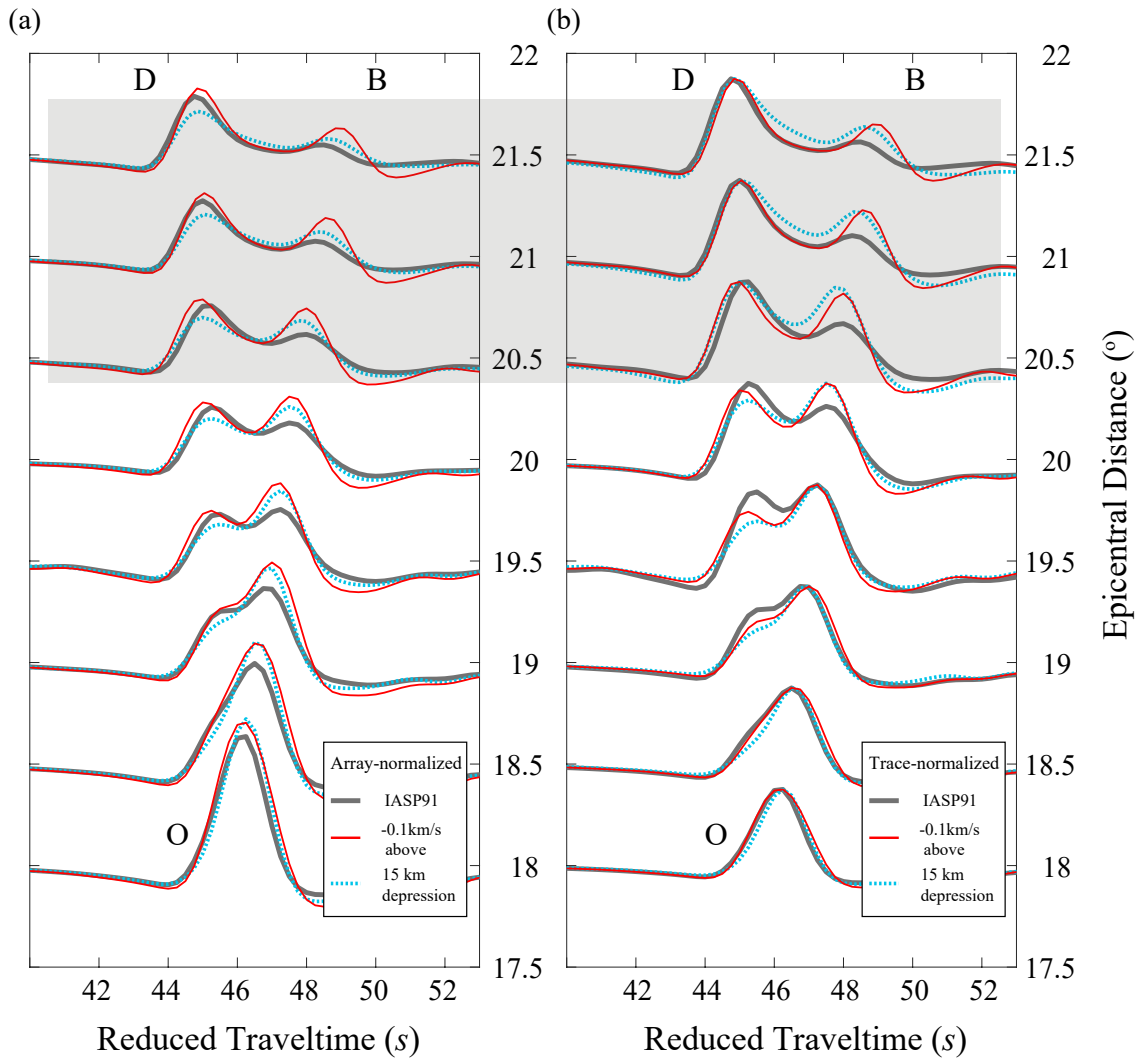


**Figure 3.** Comparison between array and trace normalization (model tradeoff). (a) Array-normalized waveforms. The bold grey waveforms are for the model IASP91, the solid red and the dashed blue waveforms represent the corresponding models in Fig. 2a. Differences between these two deviated models are clearly shown in the shaded grey region. (b) Trace-normalized waveforms. Symbols are the same as (a) and no obvious differences exist between these two models (red and blue).

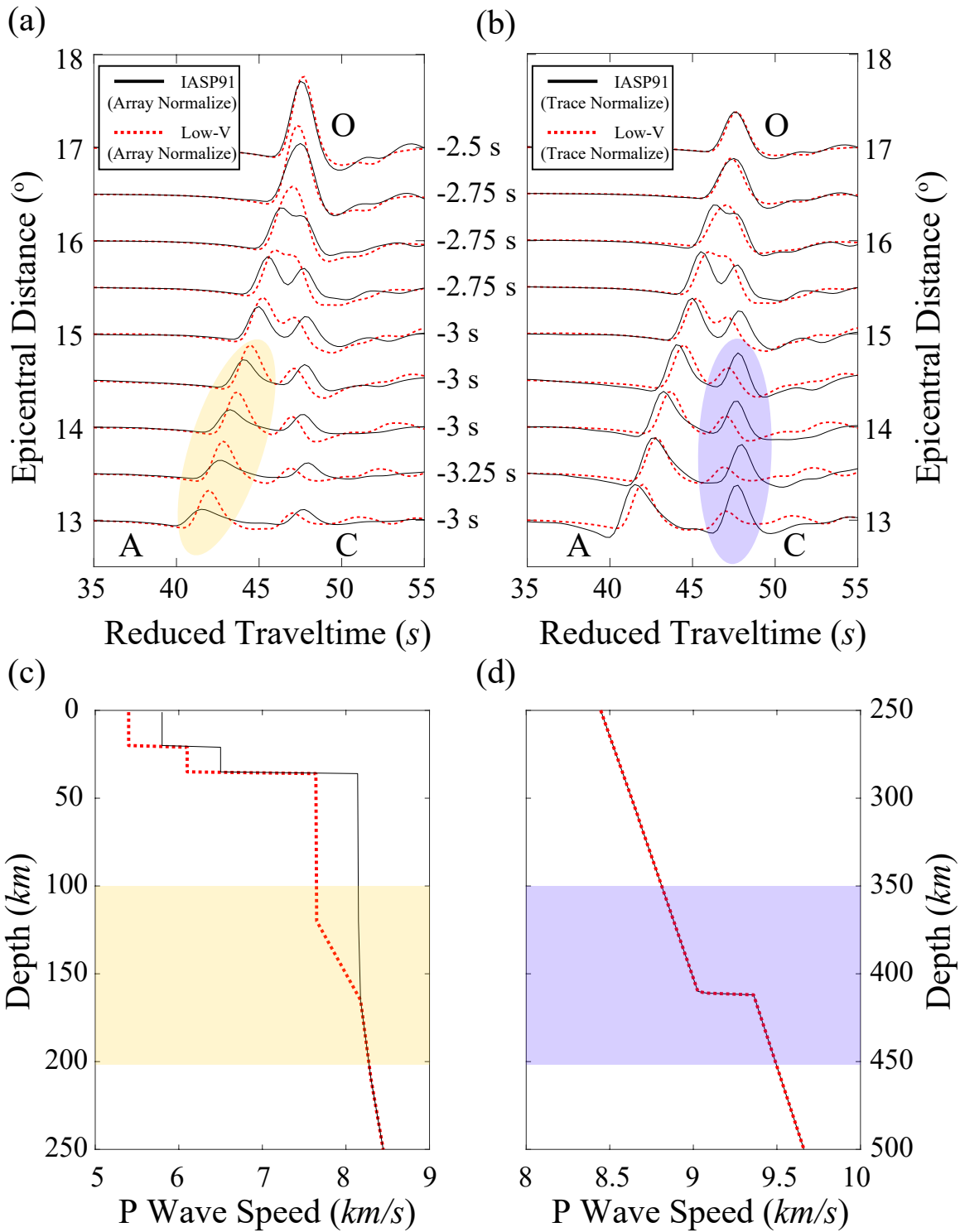


**Figure 4.** Comparison between array and trace normalization (artificial mismatch). The solid black waveforms are synthetics for the model IASP91 and the dashed red waveforms represent the red model in (c). The yellow region shows where the amplitudes are different. The number near the end of each trace denotes the time delay ( $\sim 3$  s) for each station. (b) Trace-normalized waveforms. The blue region shows where the waveforms are different. (c) The shallow portion of the model. The solid black line is the model IASP91, and the dashed red line is the designed model with a  $-0.4$  km/s zone in the top 160 km. The yellow box roughly shows where the wave speed gradient changes. (d) The deep portion of the model. The blue box roughly shows the structure we tend to modify due to the artificial mismatch of the OC branch.

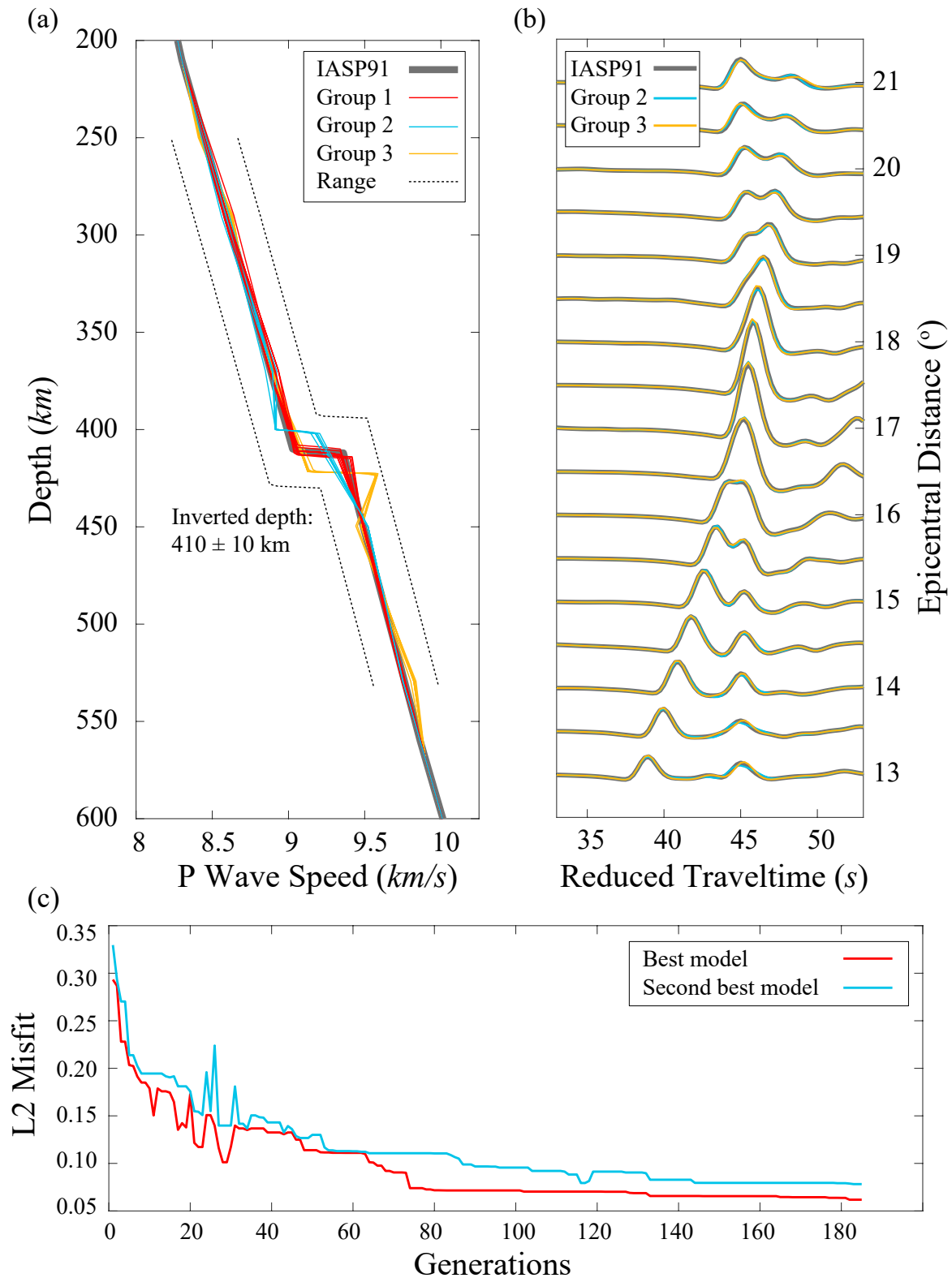


**Figure 5.** Synthetic tests for Niching Genetic Algorithm. (a) Inverted models. The bold solid grey line shows the model IASP91. The red, blue, and yellow solid lines indicate different groups of the acceptable models. The dashed black lines represent the model searching range. (b) Waveform fitting. The bold grey waveforms are synthetics for the model IASP91, the blue and yellow waveforms are synthetics using the averaged value for model group two and three, respectively. (c) L2 misfit between data and synthetics. The red and blue lines are the L2 misfit for the best and second-best models, respectively.

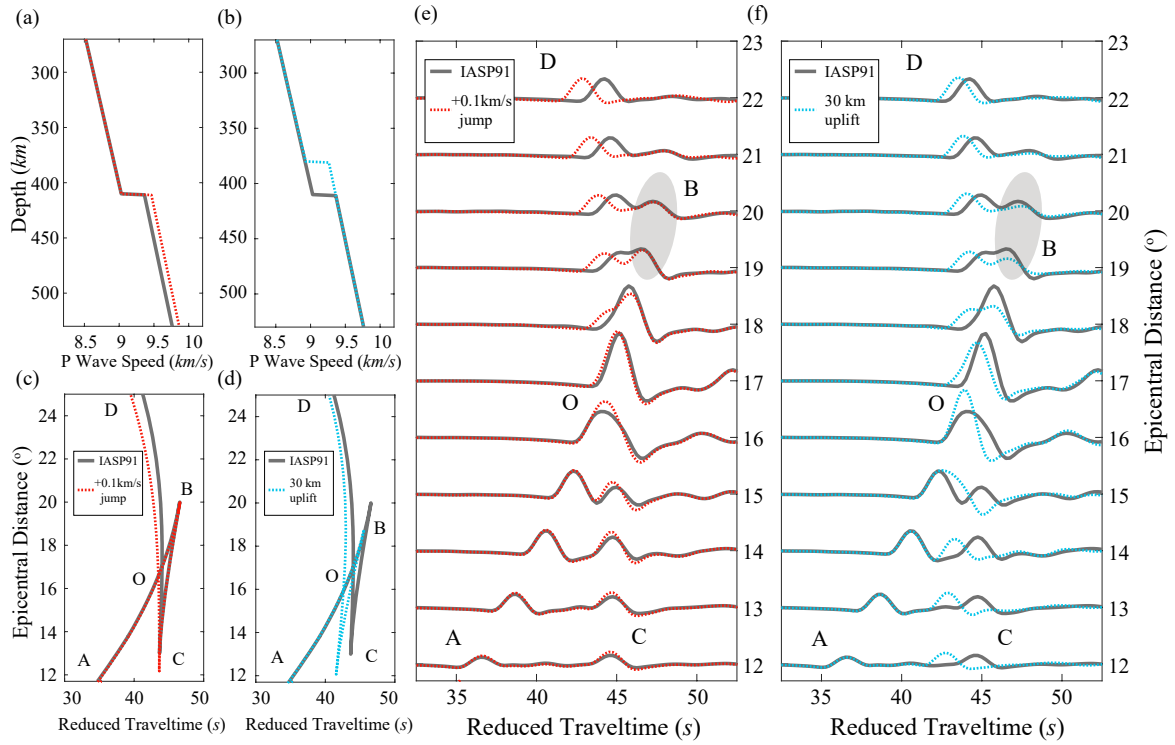


**Figure 6.** Modeling tests for the discontinuity depth and wave speed jump. (a) The bold grey line shows the model IASP91, whereas the dashed blue line is the model with a +0.1 km/s wave speed jump. (b) The model IASP91 and the model with a 30-km uplift (dashed red) . (c) Travel time curves for models in (a). (d) Travel time curves for models in (b). (e) Waveform comparison for models in (a). A reducing slowness of  $11 \text{ s}^\circ$  is applied. (f) Waveform comparison for models in (b). Grey regions in (e) and (f) indicate where the amplitude of the OB branch is different.

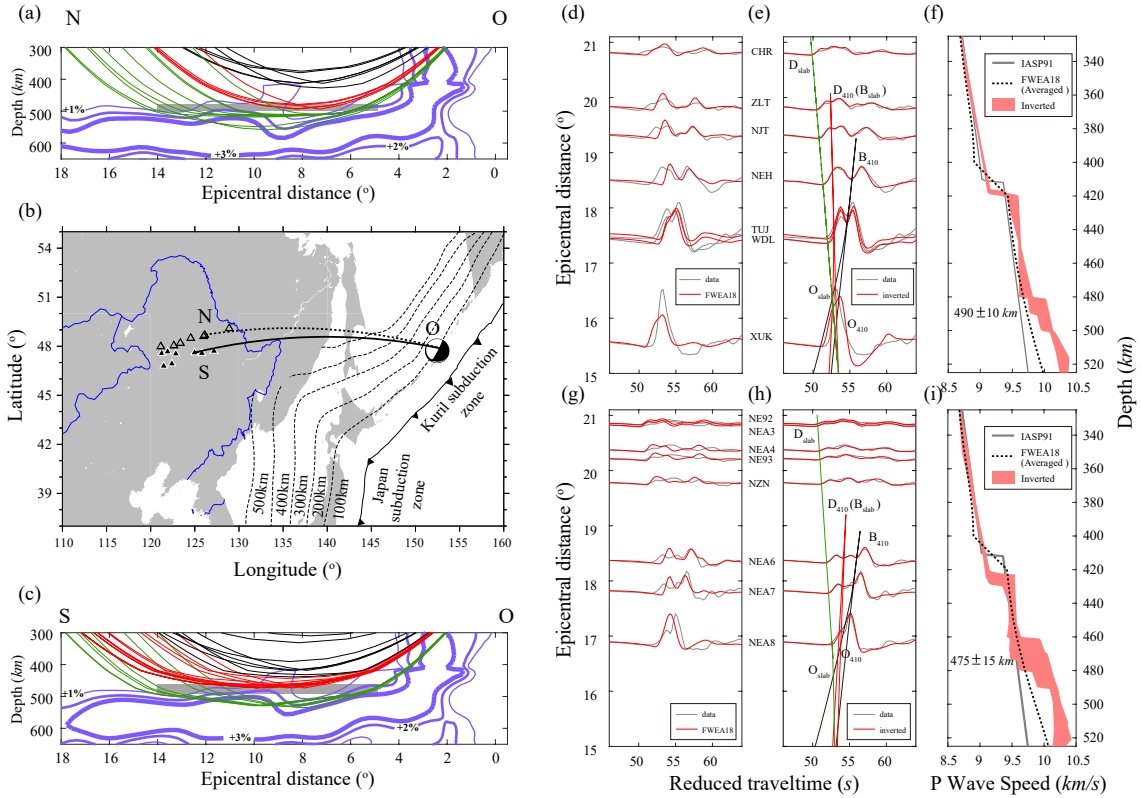


**Figure 7.** Research region and inversion results. (a) and (c) Cross-sections ON and OS as shown in (b). The blue lines are wave speed contours of the model FWEA18. The black, red, and green lines are the ray paths corresponding to the travel time curves in (e) and (h). The shaded grey regions indicate the locations of the inverted slab upper surfaces with uncertainties. (d) and (g) Displacement waveform (P wave in the Z component) comparison between aligned data (grey) and FWEA18 synthetics (red) in the northern and southern regions, respectively. A reducing slowness of  $10.5 \text{ s}^\circ$  is applied. (e) and (h) Waveform comparison between aligned data (grey) and inverted synthetics (red) for the best fitting model in the northern and southern regions, respectively. (f) and (i) P wave speed inversion models in the northern and southern regions, respectively. The shaded red region indicate all the acceptable models, whereas the solid grey line shows the model IASP91. The dashed black line represents the averaged value for the model FWEA18 (from  $5^\circ$  to  $14^\circ$ ).

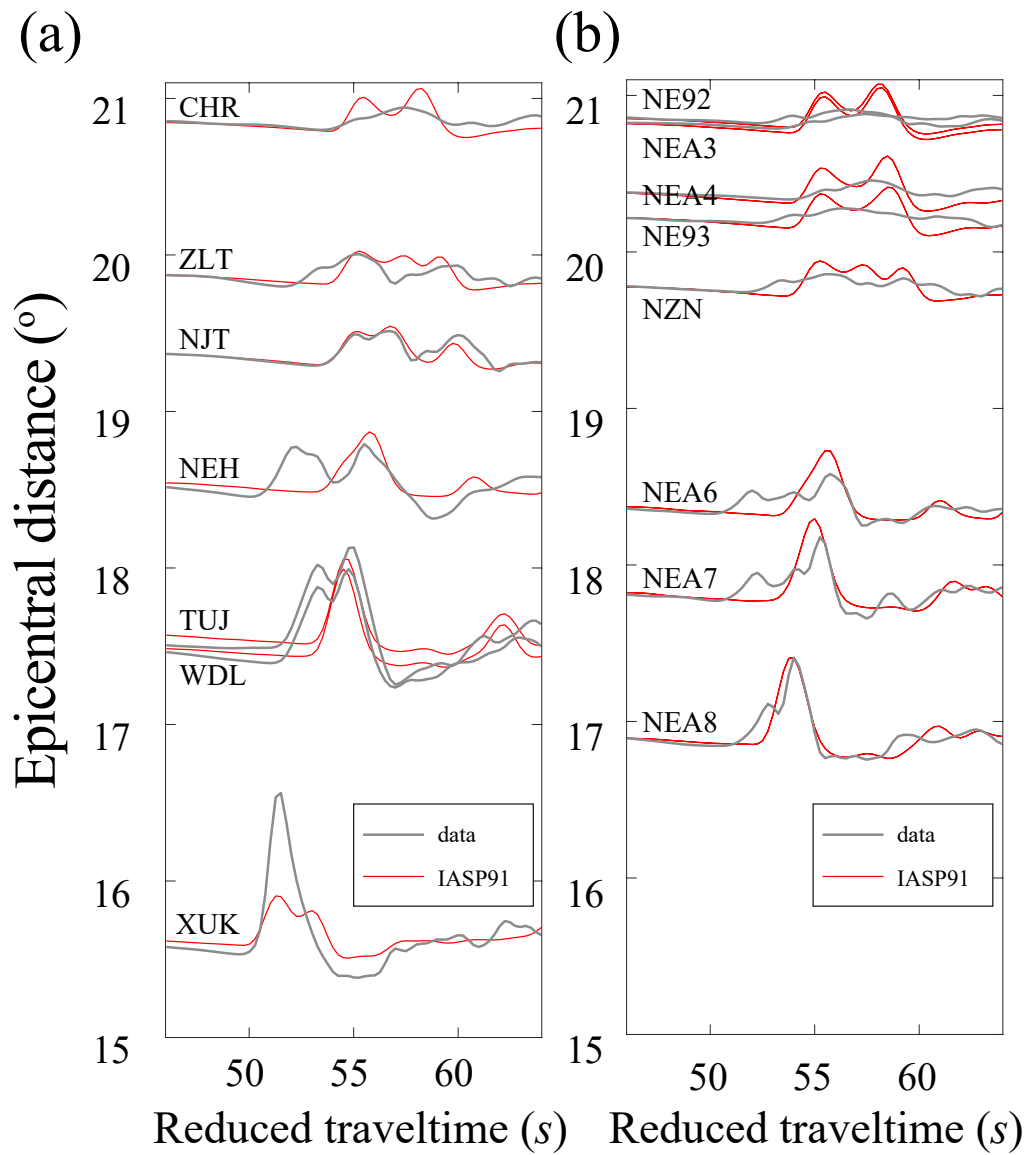


**Figure S1.** Displacement waveform comparison between aligned data (bold grey) and IASP91 synthetics (red) in the northern region (a) and southern region (b).

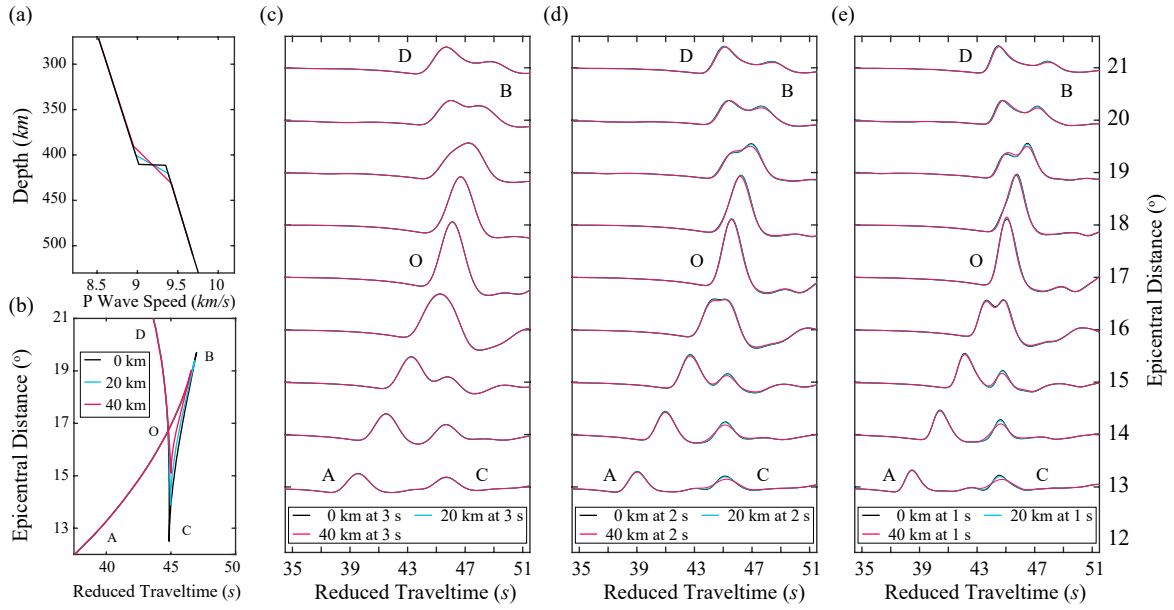


**Figure S2.** Modeling tests for the 410-km discontinuity sharpness. (a) Models used in this test. The black line is the model IAPS91, while the blue and red lines are models in which the 410-km discontinuity is replaced by a gradual transition with thicknesses of 20 km and 40 km, respectively. (b) The travel time curves for models in (a). (c) Synthetic waveforms for models in (a). Although there are significant differences in the travel time curves as shown in (b), the waveforms are almost the same with this period of 3 s. (d) Waveforms comparison with a period of 2 s. (e) Waveforms comparison with a period of 1 s. We note that for all these cases, a  $t^* \sim 1$  s is convolved.

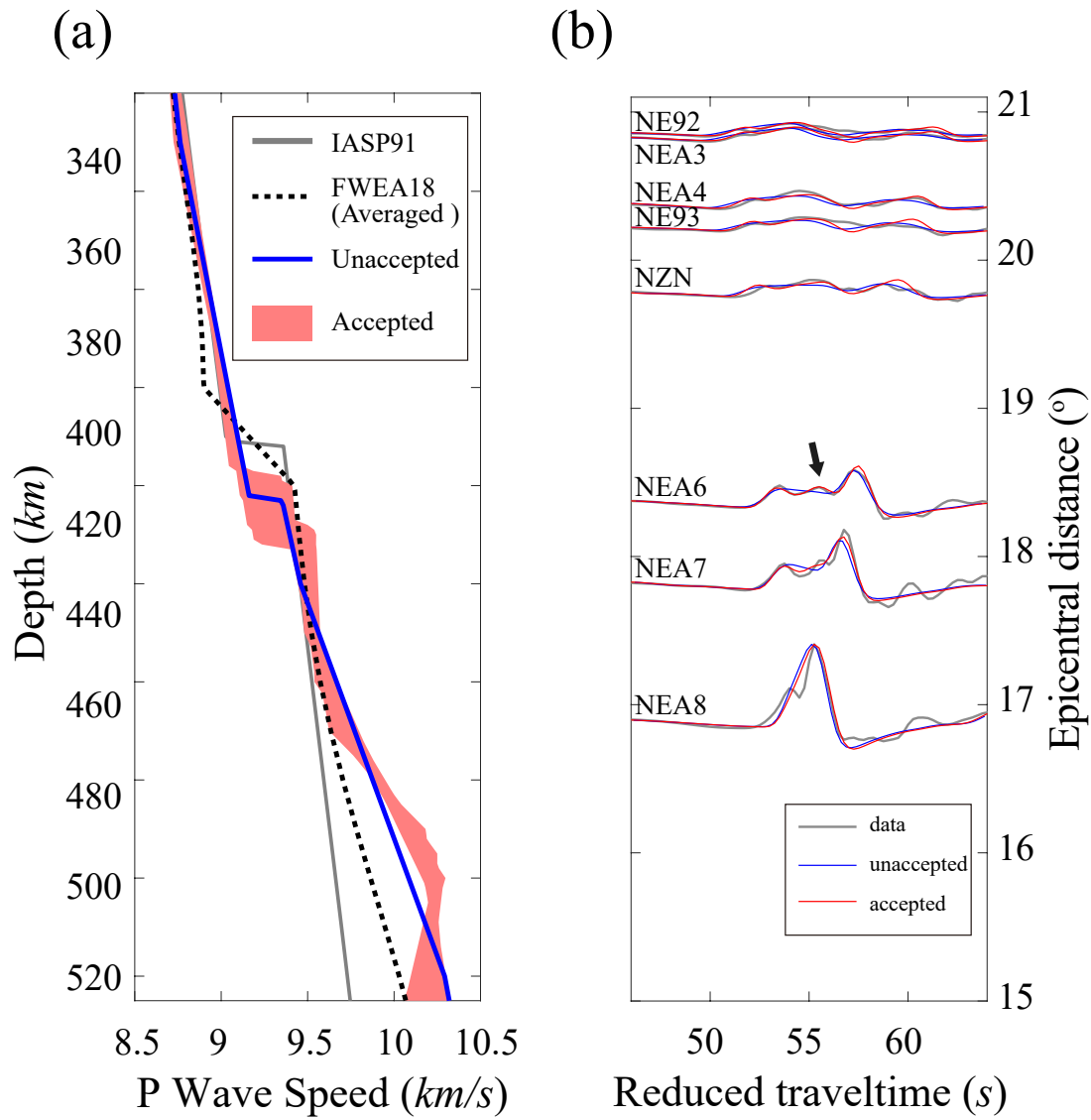


**Figure S3.** Inversion tests for slab upper surface thickness in the southern region. (a) Models. The shaded red region marks the accepted models with interface thickness from 20 km to 60 km. The bold blue line shows the unaccepted model with a thickness of 80 km. The bold grey line indicates the model IASP91. The dashed black line is the averaged value for the model FWEA18 (from  $5^\circ$  to  $14^\circ$ ). (b) Waveforms comparison between data (bold grey), and the best fitting model (red) and the model with a gradual interface of 80-km thickness (blue).



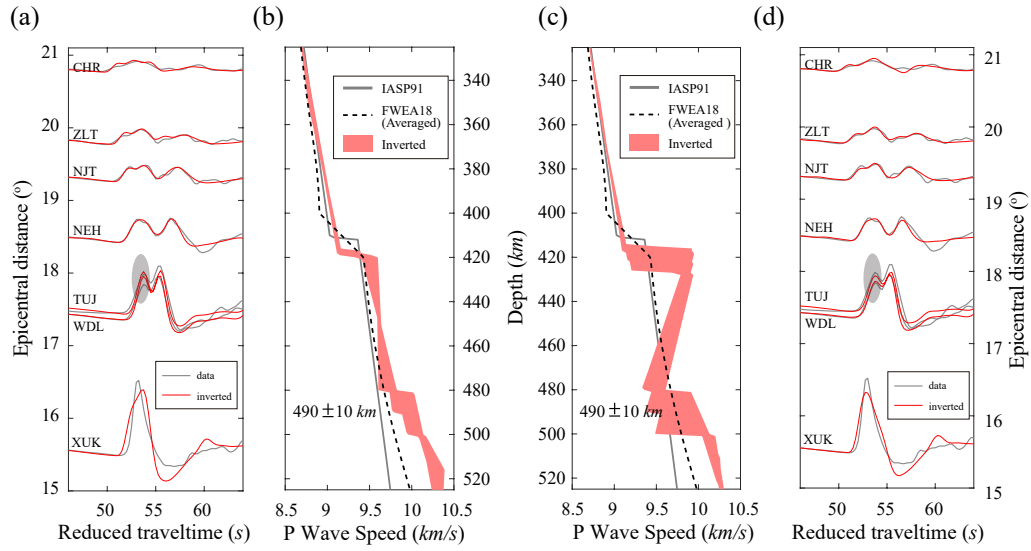


**Figure S4.** Inversion tests for the low wave speed zone in the northern region. (a) Waveforms comparison between data (bold grey), and the best fitting model (red) without a low wave speed zone. (b) The shaded red region marks the accepted models without a low wave speed zone. The solid grey line indicates the model IASP91. The dashed black line is the averaged value for the model FWEA18 (from  $5^\circ$  to  $14^\circ$ ). (c) The shaded red region marks the accepted models with a low wave speed zone between the 410-km discontinuity and the slab upper surface. Other symbols are the same as (b). (d) Waveforms comparison between data (bold grey), and the best fitting model (red) with a low wave speed zone. The grey circle indicates the waveform differences compared with (a).